

Parameters Estimation for the Cosmic Microwave Background with Bayesian Neural Networks

Héctor J. Hortúa^{1,*}, Riccardo Volpi^{1,†}, Dimitri Marinelli^{2,‡} and Luigi Malagò^{1,§}

¹*Machine Learning and Optimization Group,
Romanian Institute of Science and Technology (RIST),
Cluj-Napoca, Romania*

²*FinNet, Frankfurt am Main, Germany.*

(Dated: November 2, 2020)

In this paper, we present the first study that compares different models of Bayesian Neural Networks (BNNs) to predict the posterior distribution of the cosmological parameters directly from the Cosmic Microwave Background temperature and polarization maps. We focus our analysis on four different methods to sample the weights of the network during training: Dropout, DropConnect, Reparameterization Trick (RT), and Flipout. We find out that Flipout outperforms all other methods regardless of the architecture used, and provides tighter constraints for the cosmological parameters. Moreover we compare with MCMC posterior analysis obtaining comparable error correlation among parameters, with BNNs being orders of magnitude faster in inference, although less accurate. Thanks to the speed of the inference process with BNNs, the posterior distribution, outcome of the neural network, can be used as the initial proposal for the Markov Chain. We show that this combined approach increases the acceptance rate in the Metropolis-Hasting algorithm and accelerates the convergence of the MCMC, while reaching the same final accuracy. In the second part of the paper, we present a guide to the training and calibration of a successful multi-channel BNN for the CMB temperature and polarization map. We show how tuning the regularization parameter for the standard deviation of the approximate posterior on the weights in Flipout and RT we can produce unbiased and reliable uncertainty estimates, i.e., the regularizer acts like a hyperparameter analogous to the dropout rate in Dropout. The best performances are nevertheless achieved with a more convenient method, in which the network parameters are let free during training to achieve the best uncalibrated performances, and then the confidence intervals are calibrated in a subsequent phase. Additionally, we describe existing strategies for calibrating the networks and propose new ones. Finally, we show how polarization, when combined with the temperature in a unique multi-channel tensor fed to a single BNN, helps to break degeneracies among parameters and provides stringent constraints. The results reported in the paper can be extended to other cosmological datasets in order to capture features that can be extracted directly from the raw data, such as non-Gaussianity or foreground emissions.

I. INTRODUCTION

The Cosmic Microwave Background (CMB) is by far one of the most powerful datasets available in cosmology for understanding the Universe [1, 2]. Measurements within the last decade have yielded strong support for the standard cosmological spatially-flat Λ CDM model and provided precise estimates for its cosmological parameters [3–5]. This base model is described by six parameters divided into two groups: the *primordial* given by (n_s, A_s) that describe the initial state of the perturbations produced by quantum fluctuation during inflation, and the *late-time* group formed by $(\omega_c, \omega_b, \tau, \theta_{MC})$ which trace the linear evolution of the perturbations after re-entering the Hubble radius [6, 7]. In addition to the standard cosmological model, other parameters might provide a wealth of new information on cosmology, e.g., the total

mass of neutrinos, the effective extra relativistic degrees of freedom, the tensor-to-scalar ratio, non-Gaussianity parameters, among the others [8–12]. Such parameters have been of great interest for cosmologists because they could produce significant departures from the standard model and represent new physics in the early Universe. Combining the next-generation of CMB experiments along with large scale structure (LSS) probes will be the next step toward a precision cosmology that will allow us to constrain these fundamental physics parameters and find out extensions to the Λ CDM model [13]. However, the combination of these probes will also require more advanced statistical methods to analyze the dataset and an enormous computational effort. In fact, the estimation of the cosmological parameters demands the calculation of theoretical power spectra which are obtained through Einstein-Boltzmann Solvers (EBS) like CLASS [14][15]. Usually, these codes require few seconds for computing the observables, depending on the complexity of the cosmological model. Afterward, a comparison between the predictions at various points in the parameter space with the available observations is done, and based on the likelihood a best-fit of the parameters is obtained. Packages

* hortua.orjuela@rist.ro

† volpi@rist.ro

‡ dm@financial-networks.eu

§ malago@rist.ro

like `cobaya` [16] or `montepython` [17] use MCMC algorithms to sample from the posterior distribution and fulfil this task [18]. However, this process is computationally expensive for theoretical models that include large amount of parameters or contain “slow parameters” (most of them are late-time and delay the calculation of the power spectrum), since the EBS is executed at each step in the parameter space.

In recent years, deep neural networks have been used successfully in the field of cosmology as a way to confront the upcoming computational challenges. Originally inspired by neurobiology, deep neural network models have become a powerful tool in machine learning due to their capacity of approximating functions and dynamics by learning from examples [19, 20]. Using deep learning methods as emulators for computing the cosmological observables has become a very popular application in cosmology. Different authors have proposed to implement deep neural networks emulators for the EBS [21][22], either totally or even partially, i.e., only in places where traditional estimations are more time-consuming [23, 24]. Deep neural networks have also been used for extracting the observables directly from the raw data without requiring the power spectrum or other compressed information. Based on this strategy, deep learning has been employed in classification tasks for detecting strongly lensed systems [25, 26], discriminating cosmological models [27, 28], or detecting cosmic strings in the CMB maps [29]. Additionally, for regression tasks deep learning provides a way to make inference either in gravitational lensing systems [30, 31], weak lensing or LSS data [32–34], reionization and 21cm observations [35, 36], and CMB data [37–40], also in generative models as a powerful alternative to cosmological numerical simulations [41]. However, the use of deep neural networks may rise some problems. Indeed neural networks are prone to over-fitting, so analyzing the results only based on point estimates might produce unreliable predictions with spuriously high confidence [42, 43]. Therefore, the following question naturally arises: *how can we be sure that our model is certain about its outcomes?* This fundamental concern has been an object of study in the machine learning community and one of the most attractive approaches to address this issue relies on the use of Bayesian Neural Networks (BNNs) [44]. BNNs represent the probabilistic version of the traditional neural networks capturing the posterior probability of the outcomes and estimating their predictive uncertainties. One of the most popular techniques used to obtain the uncertainties in the Bayesian framework is called Dropout. Initially, Dropout was proposed in [45] as a regularisation scheme, subsequently the authors in [44] developed a theoretical framework in which Dropout in neural networks can be interpreted as approximate variational inference for deep Gaussian processes. Applications of BNNs using Dropout in cosmology are shown in [31, 37, 46]. Recent studies (see [47] and references therein) have found that other techniques can remarkably improve the performances of BNNs and reduce the variance of the estimates. Further-

more, in [48] the authors have claimed that Dropout fails in some architectures while others have discussed the reliability of this method [49]. Moreover, in general neural networks predictions suffer from a poor calibration over their uncertainty estimations and tend to be overconfident in their predictions, i.e., predicted posterior distributions do not reflect actual correctness probabilities [50]. Different strategies and metrics have been proposed to calibrate these networks and to be able to evaluate the accuracy of the obtained uncertainties, some of these methods will be analyzed in this paper. Based on the aforementioned discussion, our goal is twofold. Firstly, we want to show an appealing application of deep learning in cosmology by estimating the posterior distribution of the cosmological parameters directly from simulated CMB maps. Secondly, we want to describe different techniques employed to generate reliable uncertainty estimates of the predicted parameters and discuss their performance for the CMB dataset. The paper is organized as follows. First, in Sec. II, we present a motivating example for the use of Bayesian Neural Networks in Cosmology. We present a fair comparison between BNNs and MCMC posterior analysis, and we show how these approaches can also be combined to obtain the best of both worlds. In the following part of the paper we present a guide to the training and calibration of a successful BNN for the CMB temperature and polarization map. In Sec. III we describe the two sources of uncertainty in Bayesian neural networks: aleatoric and epistemic, and their importance for quantifying confidence intervals. In Sec. IV we briefly summarize the framework of variational inference, and how to produce estimates of the uncertainties and correlations of the physical parameters. Sec. V contains a description of different methods used in the literature to approximate the posterior over the weights of the networks. Some of them have been frequently used because of their simplicity of implementation, while other more recent techniques lead to better interpretation under the Bayesian framework and to improved performance. We then describe the generation of the synthetic maps used to train the inference models, including the network architectures, in Sec. VI. In Sec. VII we discuss the calibration methods used to assess the reliability of uncertainty estimates, and in Sec. VIII we show our main results related to use of BNNs in a cosmological context, as well as the credible cosmological parameter contours for our model. Furthermore, we show how the results are improved when we include polarization maps as additional channels in the images and we describe preliminary methods for network calibrations. Finally, we present our conclusions and final remarks in Sec. IX.

II. BAYESIAN INFERENCE PROBLEM: MCMC AND VARIATIONAL INFERENCE

Bayesian inference offers a way for learning from data through the posterior distribution $p(\theta|d) \sim p(d|\theta)p(\theta)$;

being θ a set of unknown parameters of interest, d the data associated with a measurement, $p(\theta)$ the prior distribution that quantifies what we know about θ before observing any data, and $p(d|\theta)$ is the likelihood function. Computing the true posterior is generally intractable, and approximation methods must be implemented in order to perform Bayesian inference in practice. Two main techniques for this purpose are Variational Inference and Markov Chain Monte Carlo (MCMC) [51–54]. The former method although is computationally faster, it requires the approximation of the true posterior (see detailed description in Sec. IV). The latter has become one of the most popular methods for cosmological parameter estimation due to its advantage of being non-parametric and asymptotically exact. Classical MCMC methods draw samples sequentially according to a probabilistic algorithm that allows to scale linearly with the dimension of the parameter space [55]. However if the complexity of the model increases either by the presence of "slow" parameters, nuisance parameters related to instrument beam response, foregrounds or parameter correlations, the sampling will exhibit a high numerical cost [56]. Additionally, it is generally difficult to determine a convenient initial state for the system and an accurate criterion to determine the convergence of the Markov Chain. These practical issues compel MCMC practitioners to resort on MCMC convergence diagnostic tools and having to wait a long time to obtain good solutions [57]. In order to make a fair comparison between both inference procedures, we will use synthetic images (small patches of CMB maps) drawn from our model described in Sec. VI. While MCMC takes in input the power spectrum extracted from the CMB maps (as it is standard practice in cosmology), VI estimates the cosmological parameters directly from the raw maps themselves. This allows the Network to adaptively extract complicated correlations when performing inference without assuming a priori summary statistics such as power spectrum or higher order spectra (such as bispectrum, trispectrum or others). For MCMC sampling we use the package cobaya, with the likelihood given by [55]

$$-\mathcal{L} \sim \sum_l (2l+1) \left[\ln \left(\frac{C_l^{BB}}{\hat{C}_l^{BB}} \left(\frac{C_l^{TT} C_l^{EE} - (C_l^{TE})^2}{\hat{C}_l^{TT} \hat{C}_l^{EE} - (\hat{C}_l^{TE})^2} \right) \right) + \frac{\hat{C}_l^{BB}}{C_l^{BB}} + \frac{\hat{C}_l^{TT} C_l^{EE} + C_l^{TT} \hat{C}_l^{EE} - 2\hat{C}_l^{TE} C_l^{TE}}{C_l^{TT} C_l^{EE} - (C_l^{TE})^2} \right], (1)$$

where \hat{C}_l is the power spectrum of the CMB map, in case of the full-sky is obtained from healpy [58], while in case of a patch is obtained by azimuthal averaging in Fourier space with Lens-Tools [59], and C_l is the theoretical model. Cobaya accepts the cosmological parameters as input, compute C_l via CLASS and when the Markov chains have enough points to provide reasonable samples from the posterior distributions, the simulation stops and it return the chains. The results are displayed in Fig. 1 where we compared the MCMC results with the best calibrated BNN model reported in Sec. VIII E (VGG-neural net

using Flipout as sampling weight method and calibrated after training).

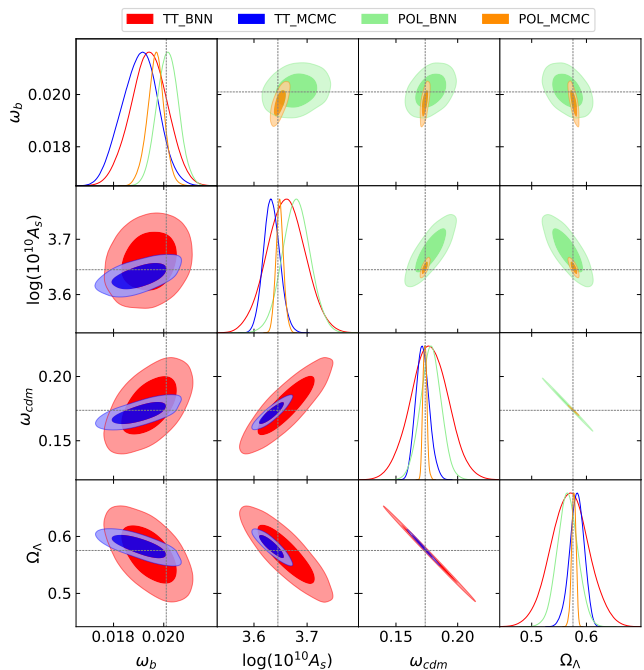


FIG. 1. Marginalized parameter constraints obtained from temperature maps (TT) and combined temperature with polarization (POL) using MCMC and the best Bayesian Neural Network (BNN) model reported in this paper. The latter model is calibrated using the method proposed in Sec. VIII E. The black line stand for the real value: $\omega_b = 0.0201$, $\log(10^{10} A_s) = 3.6450$ and $\omega_{cdm} = 0.1736$ taken from the test dataset.

Statistics for various MCMC sampling configurations						
Metrics	Map	Temperature		Temperature+Polarization		
		MCMC	covarBNN	MCMC	covarBNN	Full-sky
ω_b		0.0190 ^{+0.0013} _{-0.0013}	0.0190 ^{+0.0012} _{-0.0012}	0.01967 ^{+0.00066} _{-0.00066}	0.01968 ^{+0.00064} _{-0.00064}	0.02009 ^{+0.00010} _{-0.00010}
$\ln(10^{10} A_s)$		3.633 ^{+0.031} _{-0.031}	3.633 ^{+0.031} _{-0.030}	3.648 ^{+0.015} _{-0.015}	3.648 ^{+0.015} _{-0.016}	3.6449 ^{+0.0027} _{-0.0027}
ω_{cdm}		0.171 ^{+0.011} _{-0.011}	0.170 ^{+0.011} _{-0.011}	0.1734 ^{+0.0031} _{-0.0032}	0.1734 ^{+0.0031} _{-0.0031}	0.1736 ^{+0.0009} _{-0.0009}
Ω_Λ		0.583 ^{+0.025} _{-0.025}	0.583 ^{+0.024} _{-0.025}	0.5769 ^{+0.0079} _{-0.0080}	0.5769 ^{+0.0079} _{-0.0079}	0.5793 ^{+0.0019} _{-0.0019}
Runtime		4.02hr	1.56hr	4.40hr	3.14hr	4.52hr// 3.15hr
Acc. rate		0.19	0.23	0.14	0.25	0.18// 0.23
$R-1$		0.0093	0.0098	0.0051	0.0084	0.0091// 0.0090
$(R-1)_{95\%CL}$		0.0827	0.0764	0.0944	0.0642	0.0940// 0.0800

TABLE I. Statistics and Parameters 95% intervals for the minimal base- Λ CDM model from our synthetic CMB dataset using a non-informative priors (MCMC) and a precomputed covariance matrix from VI (covarBNN). The last column reports the metrics using the Full CMB map. The bold values in the last column correspond to the implementation of a proposal posterior distribution from VI. Although the full sky gives the smallest credible region, MCMC is 10000 times slower than VI. The real value considered is the same as specified in Fig. 1

We observe that MCMC provides tighter and more accurate constraints. However, the trained Neural Network can generate 8000 samples in approximately ten seconds which in turns out to be 10000 times faster than

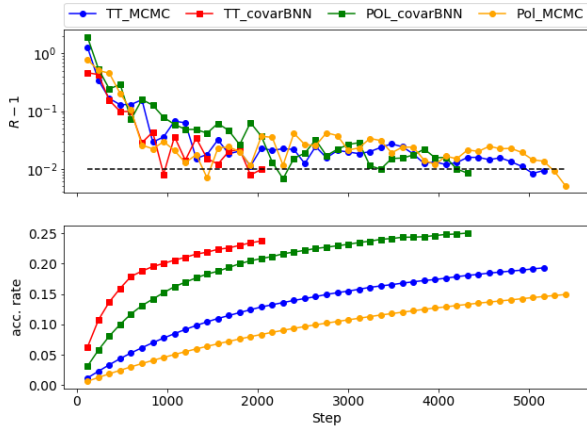


FIG. 2. *Diagnostic information on the convergence of the MCMC using unknown a priori (MCMC) and a precomputed covariance matrix from VI (covarBNN). (Top) Gelman-Rubin values with respect to the acceptance step. The black dashed line $R - 1 = 0.01$ stands for a necessary but not sufficient condition for stopping the run. (Bottom) Acceptance rate with respect to the Metropolis-Hasting step. Notice that using a proposal covariance matrix takes the MCMC reaches a higher acceptance rate in a lower number of steps.*

MCMC for this dataset [60]. Runtime and metrics for convergence in MCMC are shown in Table I. As expected, the polarization combined with temperature data shifts the values obtained from temperature alone and enhances the accuracy in all parameters (columns 1 and 3). Furthermore, a well-converged chain is also observed via the Gelman-Rubin $R - 1$ parameter and its standard deviation at 95% confidence level interval $(R - 1)_{95\%CL}$ (the smaller the better), so that the posterior is accurately measured. The qualitative correlations among parameters as obtained from BNNs are mostly analogous to the MCMC ones (Fig. 1), showing that a multi-channel BNN is able to handle the complexities involved in this kind of analysis and additionally to use the polarization information to break cosmological degeneracies. Nonetheless, although the MCMC is still 10000 times slower, it is able to better quantify the uncertainty. This is especially true when using the power spectrum of the full map, and the intervals are an order of magnitude more accurate than those computed by VI (rightmost column of Table I). It would be interesting (and more of a fair comparison) to compare MCMC for a full sky with respect to spherical neural architectures [28, 39] which can extract large scale signals correlations, thus determining if Deep Learning methods can achieve a similar level of accuracy to MCMC. On the other hand, we can also combine MCMC and VI leveraging the advantages of both methods. Such topic has attracted a lot of attention in the recent literature [61, 62]. A straightforward approach to speed up MCMC algorithms in big data problems con-

sists in using the covariance matrix constructed from the chains of the trained Neural Network as proposal for the distribution of the MCMC. In fact, it is known that a good estimate of the covariance matrix for the parameters increases the acceptance rate leading to significantly faster convergence [56]. In Table I, we compare the runtime for the MCMC with and without a precomputed covariance obtained from BNN. As we can see from the table, proposal covariances from BNNs (covarBNN) speed up convergence in MCMC reducing the computational time for all datasets (Temperature, Polarization and full sky maps). In Fig. 2 we report MCMC convergence diagnostic quantities such as $R - 1$ and the acceptance rate per iteration. The stopping rule implemented in cobaya ensures that the Gelman-Rubin $R - 1$ value and its standard deviation at 95% confidence level interval $(R - 1)_{95\%CL}$ computed from different chains (four in our case), satisfy the convergence criterion $R - 1 < 0.01$ twice in a row, and $(R - 1)_{95\%CL} < 0.2$ respectively to stop the run [16]. For the Temperature signal alone, the Markov chains achieve a steady state in about 2000 steps working with the covarBNN proposal while it usually takes more than 5000 steps instead with the vanilla MCMC. This finding can also be explained by observing the acceptance rate in Fig. 2 (bottom), this value quickly approximates to around 0.23 allowing for a reasonably high acceptance probability (For more details see [63]). An analogous trend can be seen for the polarization case. Motivated by this discussion, the use of VI in cosmological dataset for either making inference directly in the maps or as a fast-method to speed up the MCMC techniques provides a promising tool in cosmology. The rest of this paper attempts to highlight the potential use and the critical questions with respect to BNN, and aims to serve as a guide for MCMC practitioners and cosmologists to the training and calibration of a BNN.

III. EPISTEMIC AND ALEATORIC UNCERTAINTY

There are many sources of uncertainty in model prediction of physical phenomena, and their nature depend on the context and the application. However, these uncertainties have been categorized in two groups: *aleatoric* and *epistemic* [64]. Aleatoric uncertainties represent the intrinsic randomness in the input dataset [65] and they can be reduced enhancing the quality of the data. Moreover, this uncertainty can be *heteroscedastic*, i.e., the variability of the residuals does vary as the independent variables do, or the uncertainty can be *homoscedastic* when it does not.

For any neural network, the aleatoric uncertainty can be obtained by computing the variance of the conditional distribution of the predictions given the features [66]. If such conditional distribution is Gaussian, the output of the network can be split into mean predictions and their variance. Then, the variance can be learned implicitly

from the minimization of the Gaussian log-likelihood while we supervise the learning of the regression task [51, 65]. Further methods to estimate and model the aleatoric uncertainty are given in [37, 66–68].

On the other hand, epistemic uncertainty quantifies the ignorance about the correct model that generated the data, it includes the uncertainty in the model, parameters, and convergence, among the others [64]. This uncertainty is caused by the limited training data with respect to the entire feature space. Collecting more data in regions where there is a low density of training examples will reduce this uncertainty, while the aleatoric will remain unchanged [65]. Methods for estimating epistemic uncertainties are different from the aleatoric ones, and this is where BNNs can offer a mathematically grounded base for computing this uncertainty and be able to estimate the performance of the model [65]. Alternatives techniques for obtaining this uncertainty can be seen in [69]. Deep neural networks involve both types of uncertainties and determining whether a particular uncertainty is aleatoric or epistemic but sometimes could be confused [64]. However, for BNNs the authors in [70–72] rewrote the estimator for the variance such that it can be split in two terms associated to the epistemic and the aleatoric uncertainties. We will see in the Sec. VIII that this split allows us to evaluate the quality of the predictive uncertainty estimates. A more complete discussion of the nature of uncertainties can be found in [64].

IV. CAPTURING UNCERTAINTY IN NEURAL NETWORK INFERENCE

In this section we will briefly introduce some variational inference techniques to deal with non-tractable posterior distributions. We remind the reader to refer to [51, 65, 70] for additional details.

Let $\mathcal{D} = \{(\mathbf{x}_1, \mathbf{y}_1), \dots, (\mathbf{x}_D, \mathbf{y}_D)\}$ be a dataset formed by D couples of inputs $\mathbf{x}_i \in \mathbb{R}^M$ and their respective targets $\mathbf{y}_i \in \mathbb{R}^N$, and $f_W(\mathbf{x})$ be the output of the neural network with parameters (weights and biases) $\mathbf{w} \in \Omega$, where Ω is the parameter space.

Neural networks are commonly trained by Maximum Likelihood Estimation (MLE), i.e., the parameters \mathbf{w} are estimated in such a way that the likelihood of the observations in \mathcal{D} is maximized. In the Bayesian setting, we choose a prior on the weights $p(W)$, and a model which allows the definition of the likelihood $p(\mathbf{y}|\mathbf{x}, \mathbf{w})$ capturing the predictive probability of the model given \mathbf{w} . The aim then is to find the posterior distribution given the observed dataset $p(\mathbf{w}|\mathcal{D})$, which using Bayes' theorem can be written as

$$p(\mathbf{w}|\mathcal{D}) = \frac{p(\mathcal{D}|\mathbf{w})p(\mathbf{w})}{p(\mathcal{D})} = \frac{\prod_{i=1}^D p(\mathbf{y}_i|\mathbf{x}_i, \mathbf{w})p(\mathbf{x}_i)p(\mathbf{w})}{p(\mathcal{D})} \quad (2)$$

where $p(\mathcal{D}) = \int_{\Omega} p(\mathcal{D}, \mathbf{w})d\mathbf{w}$ is the evidence, and the second equality holds assuming that \mathcal{D} is a realization

of i.i.d. random variables [70]. Once the posterior has been computed, the probability distribution of \mathbf{y}^* for a new input \mathbf{x}^* can be obtained by integrating out the parameters \mathbf{w} as

$$p(\mathbf{y}^*|\mathbf{x}^*, \mathcal{D}) = \int_{\Omega} p(\mathbf{y}^*|\mathbf{x}^*, \mathbf{w})p(\mathbf{w}|\mathcal{D})d\mathbf{w}. \quad (3)$$

Unfortunately, the posterior $p(\mathbf{w}|\mathcal{D})$ usually cannot be obtained analytically and thus approximate methods are commonly used to perform the inference task. Here we will focus on a variational inference approach which approximates the posterior distribution $p(\mathbf{w}|\mathcal{D})$ by an variational distribution $q(\mathbf{w}|\boldsymbol{\theta})$, chosen in a well behaved functional space and depending on a set of variational parameters $\boldsymbol{\theta}$. The objective can then be formalized as finding $\boldsymbol{\theta}$ that makes q as close as possible to the true posterior, for instance by minimizing the KullBack-Leibler (KL) divergence between the two distributions

$$\text{KL}(q(\mathbf{w}|\boldsymbol{\theta})||p(\mathbf{w}|\mathcal{D})) \equiv \int_{\Omega} q(\mathbf{w}|\boldsymbol{\theta}) \ln \frac{q(\mathbf{w}|\boldsymbol{\theta})}{p(\mathbf{w}|\mathcal{D})} d\mathbf{w}. \quad (4)$$

By substituting the true posterior given in Eq. (2) into Eq. (4), we can observe that minimizing the KL divergence is equivalent to minimizing the following objective function

$$\begin{aligned} \mathcal{F}(\mathcal{D}, \boldsymbol{\theta}) &= \text{KL}(q(\mathbf{w}|\boldsymbol{\theta})||p(\mathbf{w})) \\ &- \sum_{(\mathbf{x}, \mathbf{y}) \in \mathcal{D}} \int_{\Omega} q(\mathbf{w}|\boldsymbol{\theta}) \ln p(\mathbf{y}|\mathbf{x}, \mathbf{w})d\mathbf{w}, \end{aligned} \quad (5)$$

which is often known as the variational free energy [51]. The first term is the KL divergence between the variational distribution and the prior that acts as an Occam's razor term, i.e., it penalizes complexity priors, while the second term drives the variational distribution to place where the likelihood is high and the data is well explained [65]. Thus variational inference transforms Bayesian learning from an analytically intractable integration to a manageable optimization problem.

Suppose the objective function $\mathcal{F}(\mathcal{D}, \boldsymbol{\theta})$ is minimized after the network is trained for some value $\hat{\boldsymbol{\theta}}$ of the variational parameters, then Eq. (3) can be rewritten in terms of $q(\mathbf{w}|\hat{\boldsymbol{\theta}})$ as

$$q_{\hat{\boldsymbol{\theta}}}(\mathbf{y}^*|\mathbf{x}^*) = \int_{\Omega} p(\mathbf{y}^*|\mathbf{x}^*, \mathbf{w})q(\mathbf{w}|\hat{\boldsymbol{\theta}})d\mathbf{w}, \quad (6)$$

where $q_{\hat{\boldsymbol{\theta}}}$ is the approximate predictive distribution. The authors in [65] proposed an unbiased Monte-Carlo estimator for Eq. (6)

$$q_{\hat{\boldsymbol{\theta}}}(\mathbf{y}^*|\mathbf{x}^*) \approx \frac{1}{K} \sum_{k=1}^K p(\mathbf{y}^*|\mathbf{x}^*, \hat{\mathbf{w}}_k), \quad \text{with } \hat{\mathbf{w}}_k \sim q(\mathbf{w}|\hat{\boldsymbol{\theta}}), \quad (7)$$

where K is the number of samples. We can also compute the covariance of the variational predictive distribution,

for a fixed \mathbf{x}^* , by invoking the total covariance law

$$\begin{aligned} \text{Cov}_{q_{\theta}}(\mathbf{y}^*, \mathbf{y}^* | \mathbf{x}^*) &\equiv \mathbb{E}_{q_{\theta}}[\mathbf{y}^* \mathbf{y}^{*\text{T}} | \mathbf{x}^*] - \mathbb{E}_{q_{\theta}}[\mathbf{y}^* | \mathbf{x}^*] \mathbb{E}_{q_{\theta}}[\mathbf{y}^* | \mathbf{x}^*]^{\text{T}} \\ &= \int_{\Omega} \text{Cov}_p(\mathbf{y}^*, \mathbf{y}^* | \mathbf{x}^*) q(\mathbf{w} | \hat{\theta}) d\mathbf{w} + \\ &\quad + \int_{\Omega} \left[(\mathbb{E}_p[\mathbf{y}^* | \mathbf{x}^*] - \mathbb{E}_{q_{\theta}}[\mathbf{y}^* | \mathbf{x}^*]) \times \right. \\ &\quad \left. \times (\mathbb{E}_p[\mathbf{y}^* | \mathbf{x}^*] - \mathbb{E}_{q_{\theta}}[\mathbf{y}^* | \mathbf{x}^*])^{\text{T}} \right] q(\mathbf{w} | \hat{\theta}) d\mathbf{w}, \end{aligned} \quad (8)$$

where $\mathbb{E}_{q_{\theta}}[\mathbf{y} | \mathbf{x}] = \int \mathbf{y} q_{\theta}(\mathbf{y} | \mathbf{x}) d\mathbf{y}$, \mathbf{y}^{T} is the transpose of the vector \mathbf{y} , and $\mathbb{E}_p[\mathbf{y} | \mathbf{x}] = \int \mathbf{y} p(\mathbf{y} | \mathbf{x}, \mathbf{w}) d\mathbf{y}$ [70, 72]. The first term in Eq. (8) collects the variability of the output coming from the training dataset which corresponds to the aleatoric uncertainty as it was mentioned in the previous section, while the second term encodes the variability of the output coming from the model, which it should be associated to the epistemic uncertainty. Following [73–75], we assume that the last layer of the network consists of a mean vector $\boldsymbol{\mu} \in \mathbb{R}^N$ and a covariance matrix $\Sigma \in \mathbb{R}^{N(N+1)/2}$. Suppose that for a given fixed input \mathbf{x}^* , T forward passes of the network are computed, obtaining for each of them a mean vector $\boldsymbol{\mu}_t$ and a covariance matrix Σ_t . Then, an estimator for Eq. (8) can be written as

$$\widehat{\text{Cov}}(\mathbf{y}^*, \mathbf{y}^* | \mathbf{x}^*) \approx \underbrace{\frac{1}{T} \sum_{t=1}^T \Sigma_t}_{\text{Aleatoric}} + \underbrace{\frac{1}{T} \sum_{t=1}^T (\boldsymbol{\mu}_t - \bar{\boldsymbol{\mu}})(\boldsymbol{\mu}_t - \bar{\boldsymbol{\mu}})^{\text{T}}}_{\text{Epistemic}}, \quad (9)$$

with $\bar{\boldsymbol{\mu}} = \frac{1}{T} \sum_{t=1}^T \boldsymbol{\mu}_t$. Notice that in case Σ is diagonal, with $\boldsymbol{\sigma}^2 = \text{diag}(\Sigma)$, the last equation reduces to the variance of the variational predictive distribution given in [70, 73], given by the sum of both the aleatoric and the epistemic uncertainties, that is

$$\widehat{\text{Var}}(\mathbf{y}^* | \mathbf{x}^*) \approx \underbrace{\frac{1}{T} \sum_{t=1}^T \boldsymbol{\sigma}_t^2}_{\text{Aleatoric}} + \underbrace{\frac{1}{T} \sum_{t=1}^T \boldsymbol{\mu}_t^2 - \bar{\boldsymbol{\mu}}^2}_{\text{Epistemic}}. \quad (10)$$

In this setting, neural network can be used to learn the correlations between the the targets and produce estimates of their uncertainties.

V. VARIATIONAL DISTRIBUTIONS

In this section we will review different types of neural networks, all characterized by a common (aleatoric) Gaussian layer in output. After training, in deterministic neural networks (Fig. 3a) the weights have a fixed value. On the other side, in Bayesian Neural Networks (Fig. 3b) we have a prior and a posterior distribution defined over their weights (Sec. IV), which is usually chosen to belong to a well behaved family of distributions. Two

popular approximations for BNNs are Dropout and DropConnect. In Dropout (Fig. 3c) each neuron is dropped with a certain probability, while in DropConnect (Fig. 3d) the weight-connections are dropped instead. The most popular approaches for BNNs present in the literature are briefly summarized in the following.

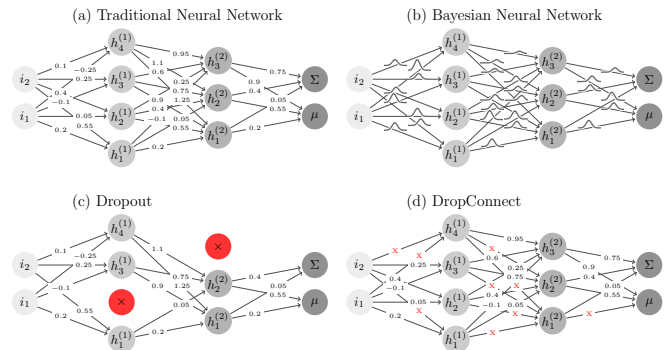


FIG. 3. Diagrammatic representation of aleatoric neural networks with a stochastic Gaussian layer in output. The nodes i correspond to the inputs of the network (e.g., the pixels of an image); the nodes h are the nodes in the hidden layers; the output of the networks are the mean and covariance of a Gaussian distribution.

A. Bernoulli via Dropout

Dropout was first proposed in [45] as a regularisation method for neural networks which helps to reduce co-adaptations amongst the neurons. During training, each neuron in the j -th layer $\mathbf{h}^{(j)}$ of size H_j is dropped from the network with probability p (commonly known as Dropout rate). The application of Dropout can be expressed as

$$\mathbf{h}^{(j+1)} = \sigma \left(\mathbf{m}^{(j+1)} \circ (W^{(j)} \mathbf{h}^{(j)}) \right), \quad \mathbf{m}^{(j+1)} \sim \text{Ber}(p), \quad (11)$$

where \circ corresponds to the Hadamard product, $\sigma(\cdot)$ is a nonlinear activation function, $W^{(j)}$ is the weight ($H_{j+1} \times H_j$)-matrix for the layer j , and $\mathbf{m}^{(j+1)}$ a vectorial mask of size H_{j+1} , which is sampled from a Bernoulli distribution with probability p . Once trained, the entire network is used although neurons are scaled using the factor $1 - p$, this compensates for the larger size of the network compared to the one used during training. Interestingly, the authors in [76] have shown a connection between Dropout and approximate variational inference for Gaussian processes, allowing the neural network to be interpreted as an approximate Bayesian model. In this case, the variational distribution $q(W^{(j)})$ for the j -th layer associated to Eq. (11) can be defined as [77]

$$W^{(j)} = V^{(j)} \text{diag} \left(\mathbf{m}^{(j)} \right), \quad \mathbf{m}^{(j)} \sim \text{Ber}(p), \quad (12)$$

being $V^{(j)}$ a ($H_{j+1} \times H_j$)-matrix of variational parameters to be optimised. Inserting this variational distri-

bution into Eq. (5), we obtain an unbiased estimator for the objective function [76]

$$-\hat{\mathcal{F}} = \sum_{i=1}^D \ln p(\mathbf{y}_i | \mathbf{x}_i, \mathbf{w}) - \lambda \sum_{j=1}^L \|W^{(j)}\|^2, \quad (13)$$

where λ is a positive constant and the weights are sampled at each layer from $q(W^{(j)})$ defined in Eq. (12). The first term corresponds to the likelihood that encourages \mathbf{w} to explain well the observed data, while the second term is a L_2 regularization, weighted by the weight decay parameter λ , which mimics the KL divergence term in Eq. (5). Therefore, training a neural network using Dropout has the same effect as minimizing the KL divergence in Eq. (4). This scheme, besides working similar to a Bayesian Neural Network, acts also as a regularization method which prevents over-fitting. After training the neural network, Dropout remains active and we follow Eqs. (7) and (9) to perform inference and estimate the uncertainties of the network. Such procedure is known in the literature as Monte Carlo Dropout.

B. Bernoulli via DropConnect

DropConnect is a generalization of Dropout used for regularization in deep neural networks [78]. In this method, each weight-connection is dropped with probability p , differently from DropConnect where instead neurons are dropped. The hidden nodes of each layer are given by

$$\mathbf{h}^{(j+1)} = \sigma \left((M^{(j)} \circ W^{(j)}) \mathbf{h}^{(j)} \right), \quad M^{(j)} \sim \text{Ber}(p), \quad (14)$$

where $M^{(j)}$ a matrix mask of size $H_{j+1} \times H_j$. In [79, 80] the authors use DropConnect to obtain approximated uncertainties. Here, the mask is applied directly to each weight, differently from Dropout where the weights are not sampled. The variational distribution for the weights of the j -th layer is defined by

$$W^{(j)} = W^{(j)} \circ M^{(j)}, \quad M^{(j)} \sim \text{Ber}(p), \quad (15)$$

where $m_{rs}^{(j)}$ is the element of the mask $M^{(j)}$ connecting the r -th neuron of the $(j+1)$ -th layer to the s -th neuron of the j -th layer. Similarly to the previous case, during training the network weights are learned to minimize Eq. (13), while at test time each input is passed through the network multiple times. DropConnect allows to capture both the epistemic and aleatoric uncertainties via Eq. (9).

C. Reparameterization Trick and Flipout

So far we have seen two methods to provide the network with stochastic weights. Dropout deals with stochastic activations (drop neurons), the weights are not sampled independently, however it is easy to implement and quite

cheap to compute. On the other hand, DropConnect drops directly the weights which in most cases are far more than the number of neurons, i.e., this method is more expensive and it has a higher variance.

Recently, different works have proposed to sample the weights from a Gaussian distributions instead. The *Reparameterization Trick* (RT) allows to generate samples which are differentiable with respect to the the parameters of the distribution from which they are drawn [81]. If the weights are considered as a continuous random variable drawn from $\mathbf{w} \sim q(\mathbf{w}|\boldsymbol{\theta})$, thanks to the RT we might express it as a deterministic function $\mathbf{w} = g(\boldsymbol{\epsilon}, \boldsymbol{\theta})$ of a fixed random auxiliary variable $\boldsymbol{\epsilon}$, i.e., $\boldsymbol{\epsilon} \sim p(\boldsymbol{\epsilon})$ has a probability density function p independent of $\boldsymbol{\theta}$, while g is parameterized by $\boldsymbol{\theta}$. This implies that any expectation with respect to $q(\mathbf{w}|\boldsymbol{\theta})$, can be estimated as [81, 82]

$$\int_{\Omega} q(\mathbf{w}|\boldsymbol{\theta}) f(\mathbf{w}) d\mathbf{w} \approx \frac{1}{K} \sum_{k=1}^K f(g(\boldsymbol{\epsilon}_k, \boldsymbol{\theta})) \quad \text{with } \boldsymbol{\epsilon}_k \sim p(\boldsymbol{\epsilon}). \quad (16)$$

In the multivariate Gaussian case $\mathbf{w} \sim \mathcal{N}(\boldsymbol{\mu}, \Sigma)$ [83], we have the usual reparameterization given by $\mathbf{w} = \boldsymbol{\mu} + L\boldsymbol{\epsilon}$, where $\boldsymbol{\epsilon} \sim \mathcal{N}(\mathbf{0}, I)$ and L has the property that $\Sigma = LL^T$, a noteworthy example being the lower triangular Cholesky factorization. Given this reparameterization along with Eq. (16), we can get the approximated value of the second term in Eq. (5) and thus it is possible to derive the unbiased estimate of the gradient of the variational free energy [81].

The downside of the RT is that the sampled weights are the same for all the examples in the batch, thus correlating the gradients between different samples in the same batch. To overcome this limitation and thus reduce the gradient variance, the authors of [47] propose the *Flipout* method as an efficient way to provide pseudo-independent weights perturbations. Methods like Flipout or Local Reparameterization Trick [82] are some of the strategies used today for variance reduction. Flipout assumes that the variational distribution can be written as a mean $\overline{W}^{(j)}$ plus a perturbation $\Delta W^{(j)}$ with symmetric distribution around zero, i.e.,

$$W^{(j)} = \overline{W}^{(j)} + \Delta W^{(j)}, \quad (17)$$

and proposes to decorrelate the noise inside a mini-batch by sampling a series of pseudo-random sign matrices, to randomly flip the symmetric perturbation of the weights. For a sample i in the batch

$$\Delta W_i^{(j)} = \widehat{\Delta W}^{(j)} \circ (\mathbf{r}_i \mathbf{s}_i^T) \quad (18)$$

where \mathbf{r}_i and \mathbf{s}_i are random vectors whose entries are uniformly sampled from $\{\pm 1\}$ and $\widehat{\Delta W}^{(j)}$ is a perturbation sampled only once for the whole mini-batch. Remarkably this approach can be easily vectorized for a given batch and used to efficiently obtain pseudo-random weights perturbations [82].

VI. DATASET AND NETWORK

We have generated 50,000 independent realizations of simulated CMB full-sky maps and extracted from them images of $20 \times 20 \text{ deg}^2$ and 256×256 pixels. From the total dataset, 70% is reserved for training, 10% for validation, and 20% for testing. These simulations have been created given the temperature angular power spectra generated by CLASS and healpy [58], by originating a realisation on the HEALPix grid. The choice of the resolution for the maps comes from the analysis displayed in Fig. 4. Here we can see that for small angular sizes, the power spectrum obtained from the patches cannot retain enough information from the original spectrum produced by CLASS, in contrast to images with angular size equal to or larger than $10 \times 10 \text{ deg}^2$. However for very larger angular size, the assumption of a good flat approximation is not valid and distortions produced by the projection of the spherical data into the flat sky could lead to undesirable effects, that is, the resolution leads to a trade-off between accuracy of the recovered power spectrum and execution time (e.g., speed) of the neural network. One alternative to deal with large angular size images is to create CMB maps from the lens-tools package [59] which produces a Gaussian random field directly over the pixels of the flat image.

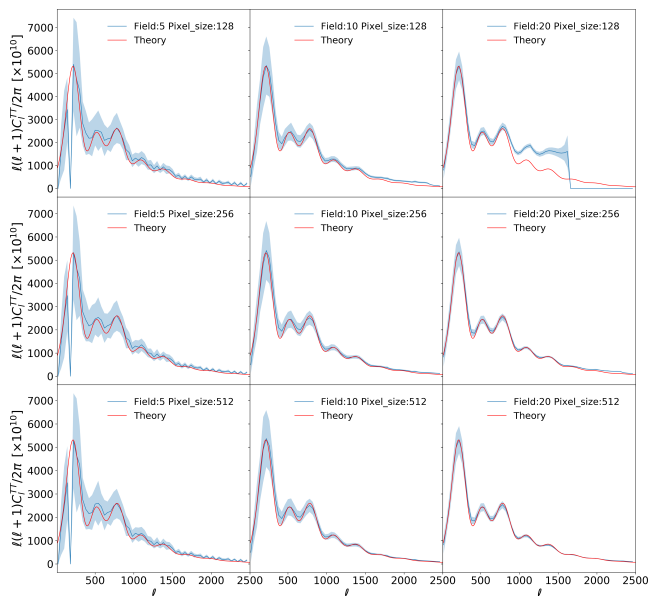


FIG. 4. Power spectra generated from patches with different angular scales (Field: $\{5, 10, 20\} \text{ deg}^2$) and pixelized into: $\{128, 256, 512\}$ pixels). The light-blue shadowed regions correspond to the standard deviation of 500 samples. The red line shows the power spectrum obtained from the theory. We have used lens-tools (using azimuthal averaging in Fourier space) to compute the power spectrum of the CMB patches [59]. The configuration used in the following section is 20 deg^2 with 256 pixels.

In this paper we assume a minimal version of the

Λ CDM model where each power spectrum generated in CLASS differs in three parameters: *baryon density* $\omega_b \in [0.019, 0.031]$, *cold dark matter density* $\omega_{cdm} \in [0.06, 0.22]$, and *primordial spectrum amplitude* $A_s \in [1.01 \times 10^{-9}, 4.01 \times 10^{-9}]$, sampled over a uniform 3D grid, while the rest of the Λ CDM parameters are fixed to the values reported by the Planck mission [7]. The multiple generations of the power spectra should gather the cosmic variance that will contribute to the aleatoric uncertainty. The images and the parameters are normalized between -1 and 1, without any additional data augmentation.

Architecture

We have implemented our models in TensorFlow [84]. The API tf.Keras and the library TensorFlow-Probability [85] have been also used for RT and Flipout, while Dropout and DropConnect were implemented in the higher-level library Sonnet [86]. We implemented a modified version of the VGG [87] and AlexNet [88] networks illustrated in Fig. 5. We have chosen to have all the architectures with roughly the same number of weights so that the analysis carried out for all BNNs depends only on their performance, and not on the size or complexity of the network. The VGG network consists of ten convolutional layers with a fixed kernel size of 3×3 , using LeakyReLU as the activation function. Each convolutional layer, except for the last one, is followed by a batch renormalization layer, which ensures that the activations computed in the forward pass during training depend only on a single example and are identical to the activations computed in test [89]. We have applied zero padding in each convolution layer, and we have downsampled using max pooling, allowing the network to learn correlations at large angular scales. For AlexNet the input is convolved with six convolutional layers of kernel size $(11, 5, 3, 3, 3, 1)$, with the same activation function after each layer, and without batch (re)normalization. The downsampling is done using max pooling for three of the six layers as we can see in Fig. 5. One critical modification with respect to AlexNet consists in the change of the fully connected layers at the end of the network which are replaced by convolutional layers. Indeed, we have observed that in our configuration, for the CMB dataset, the presence of the dense layers deteriorates the performances. At the end of the convolutional part for both architectures, a dense layer with nine neurons is built, three of them correspond to the means of the cosmological parameters used to generate the maps, and the other six compose a lower triangular matrix L [74, 75]. This last layer yields to a multivariate Gaussian distribution with mean μ and covariance $\Sigma = LL^T$ to guarantee positive definiteness.

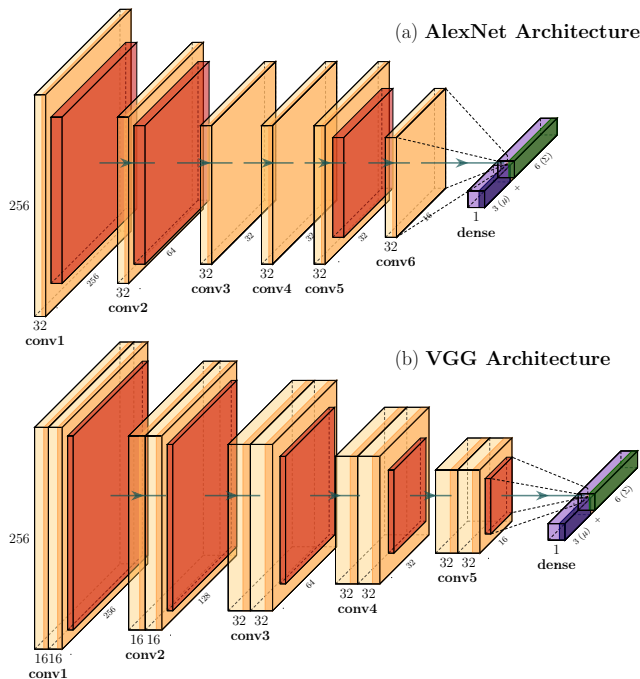


FIG. 5. Illustration for the modified versions of the (a) AlexNet and (b) VGG architectures. The input of the networks are images of 256×256 pixels and the output consists of nine values. Both architectures have around $\sim 60,000$ weights, being batch normalization in VGG the most remarkable difference between them.

Training

The negative log-likelihood (NLL) of our neural network, used to estimate the cosmological parameters and their uncertainties, is given by

$$\mathcal{L} \sim \frac{1}{2} \log |\Sigma| + \frac{1}{2} (\mathbf{y} - \boldsymbol{\mu})^\top \Sigma^{-1} (\mathbf{y} - \boldsymbol{\mu}), \quad (19)$$

averaged over the mini-batch. The objective function differs depending on the method employed. For example, for Dropout and DropConnect, it will be expressed as the sum of the negative log-likelihood in Eq. (19) plus a L2-regularization term from Eq. (13). Here we used $\lambda = 0.001$ for the weights and $\lambda = 0.0001$ for the biases.

In the case of RT and Flipout, the optimization is based on the minimization of the KL divergence written in Eq. (5). The prior that we have chosen is a normal distribution under the mean field approximation, initialized with mean 0 and variance 1, while the posterior is given by another Gaussian distribution initialized with the Glorot normal initializer for the mean, while the variance is sampled from a Gaussian distribution $\mathcal{N}(-9, 0.01)$ (before applying the Softplus function). Furthermore, the weights of the posterior are controlled by a L2-regularization term and the biases in both cases are taken as a deterministic function. Different experiments using (non)-trainable

prior distributions showed that training both the posterior and the prior parameters turned out in better performances. Furthermore, a deterministic dense layer as the last layer of the network (producing in output $\boldsymbol{\mu}$ and Σ) instead of a probabilistic one produces better results. The algorithm used to minimize the objective function is the Adam optimizer [90] with first and second moment exponential decay rates of 0.9 and 0.999, respectively, a learning rate of 10^{-4} , and decay rate of 0.9. The decay step has been tuned based on the specific method: for Flipout is 6,000, for Dropout and DropConnect is 8,000, and for RT 2,000. We trained the networks for 400 epochs with batches of 32 samples.

Validation and Test

We have fed each input image from the test set 2,500 times to each network, essentially getting enough samples from the posterior of the network and hence being able to capture the epistemic uncertainty. Each sample produces nine variables corresponding to the cosmological parameters and their covariance matrix. The latter represents the aleatoric uncertainty learned from optimizing the objective function, hence, the total uncertainty reported for each example is provided via Eq. (9).

VII. CALIBRATION

The issue of the calibration of neural networks has gained interest in the recent years, since it has been shown that deep neural networks tend to be overconfident in their predictions [91]. Different works have addressed to problem of identify why a neural network may become miscalibrated (see, e.g., [50], and references therein). One of the ways to diagnostic the quality of the uncertainty estimates is through reliability diagrams. Fig. 6 displays the confidence intervals against the expected coverage probabilities defined as the $x\%$ of samples for which the true value of the parameters falls in the $x\%$ -confidence interval. If the network is well calibrated, then the diagram should correspond to a straight line corresponding to the identity function and any deviation from it represents a miscalibration. As we will show later, the methods employed to adjust the predicted uncertainties can be applied during or after training. During the training process, we just need to adapt some hyper parameters in the model in order to achieve a good calibration. For example, in the case of Dropout the authors in [31] found out that the Dropout rate should be tuned to produce high accuracy uncertainty estimations (see AlexNet with Dropout rate 7% in Fig. 6). Moreover, the authors in [93] introduced Concrete Dropout which allows for the dropout probabilities to be automatically tuned, improving the performance and producing calibrated uncertainties. Additionally, we will show in the next section that the hyper parameters related to Flipout correspond to the regu-

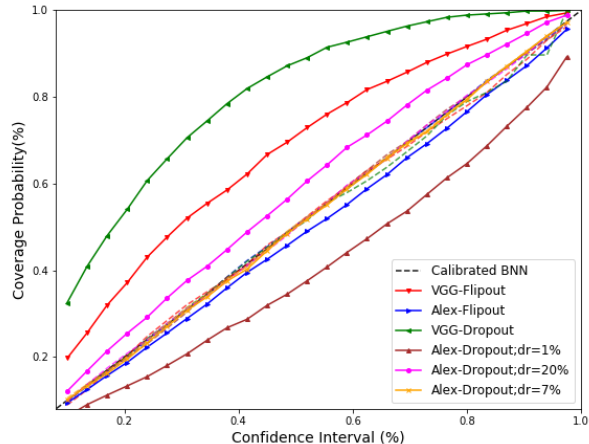


FIG. 6. Reliability diagrams for CMB maps before (solid lines with marks) and after calibration (dashed lines). The black dashed line stands for the perfect calibration, while the other color lines represent different BNNs. For some hyperparameters values in AlexNet (Alex), the model underestimates its errors, while for VGG all models are overconfident in their predictions. We have implemented beta calibration to obtain these curves [92].

larization parameters for the scale of the approximate posterior over weights and biases. However, calibrating the network during training is not efficient in all cases. Tuning the hyper parameters could drastically affect the performance of the model and besides this, the method depends strongly on the architecture of the network. An example on this issue will be shown later when we will observe that this technique fails on the VGG architecture. On the other hand, it has been noticed that methods for calibrating the network after training indeed preserve the accuracy of the predictions achieved during training. Histogram Binning [94], Isotonic Regression [95], Platt Scaling [92, 96, 97], and Temperature Scaling are some of the most common methods used for calibrating the networks for regression tasks. In this work (except in Subsec. VIII E) we will use an extended version of the parametric Platt Scaling method described in [92]. Basically, we build the reliability diagram and fit it to the calibrated map [92]

$$\beta(x; a, b, c) = \frac{1}{1 + \left(e^c \frac{x^a}{(1-x)^b} \right)^{-1}}, \quad (20)$$

with scalar parameters a , b , and $c \in \mathbb{R}$. Hence, we apply the following transformation to the covariance matrix $\Sigma \rightarrow s\Sigma$ in the evaluation of the coverage probabilities, see Eq. (21), being $s \in \mathbb{R}^+$ a scalar parameter. Finally, we choose the value of s used for the calibration of the network by minimizing the difference of the calibrated maps with respect to the diagonal line. Fig. 6 displays the

results of the beta calibration for different BNN models for VGG and AlexNet. For example, a Dropout rate of 1% using AlexNet or Flipout on AlexNet without regularization on their posterior weights will produce underestimation in their errors. This means that most of the true values do not fall in their corresponding confidence intervals, as we can see in Fig. 7. On the other hand, overconfident networks (like VGG, as we see in Fig. 6) are very conservative in their errors, therefore they produce weak confidence bounds on the parameter space, as it is shown in Fig. 7. Finally, let us discuss about the evaluation of the coverage

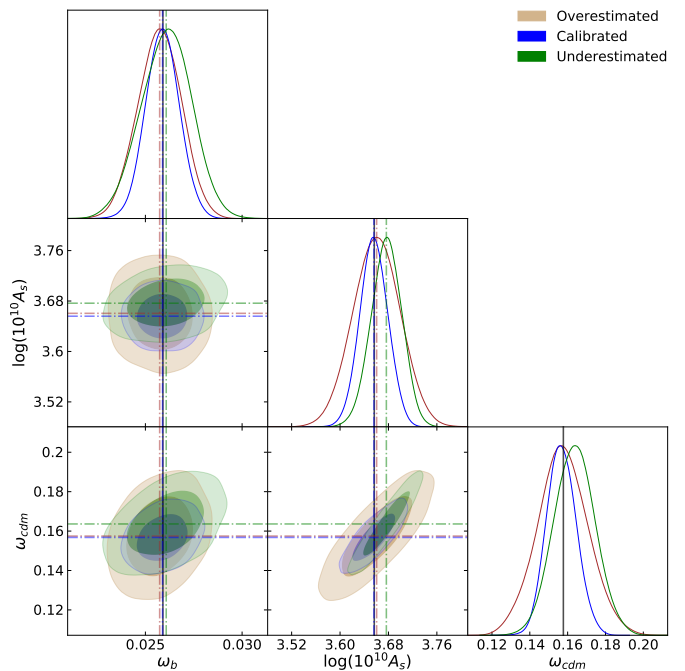


FIG. 7. Triangular plot for the 95% contours of the cosmological parameters obtained from calibrated (blue), under (green)- and over (orange)- estimated models. The black lines stand for the real value, while the dashed lines refer to their predicted values. The marginalized distributions show the behavior of miscalibrated networks compared with a calibrated one. We have used the Python GetDist package for creating the triangular plot [98].

probabilities. We have noticed how all models used in this work produce a full predictive posterior distribution (3) which is approximately Gaussian (higher order statistical moments very close to zero). Hence, treating the distribution as a multivariate Gaussian, the confidence intervals can be computed by

$$\mathcal{C} \geq (\mathbf{y} - \hat{\mathbf{y}})^\top \Sigma^{-1} (\mathbf{y} - \hat{\mathbf{y}}), \quad (21)$$

which is basically an ellipsoidal confidence set with coverage probability $1 - \alpha$. The quantity \mathcal{C} has the Hotelling's T-squared distribution $T_{k, D-k}^2(1 - \alpha)/D$, with k degrees of freedom, being D the number of samples [99]. For large samples, the Hotelling's T^2 tends to the more common

χ^2 distribution [100], which is the distribution of the sum of the squares of k independent standard normal random variables. This is indeed the distribution which we will use in the calculation of our confidence intervals. Therefore, the coverage probabilities correspond to the percentage of samples satisfying Eq. (21), in other words, the fraction of examples where the true values lay into the 3D-ellipsoidal region. This evaluation generalizes the methods in the literature in which we must bin the samples in order to estimate the region that contains $(1 - \alpha)$ of the test dataset, as long as the joint distribution is almost Gaussian. In Appendix A, we compute the coverage probabilities from the histograms as it is usually done in the literature [25], finding consistent results when we used ellipsoidal confidence intervals.

VIII. ANALYSIS AND RESULTS

In this section we describe the results we obtained with different architectures and types of BNNs. We compare all experiments in terms of performance, i.e., the precision of their predictions for the cosmological parameters quantified through Mean Square Error (MSE), and their values achieved in the NLL. Furthermore, we analyze the quality of the uncertainty estimates in each experiment and its appropriate calibration, if needed.

A. Dropout and DropConnect

We begin by comparing the performance of Dropout and DropConnect. The best results are displayed in Table II. As it can be seen, DropConnect does not exhibit particularly exciting performances for any architecture. Even for a vast range of regularization and initialization values, we could not achieve good results, as was reported in [79]. It seems that DropConnect injects large noise on convolutional layers until this unstabilizes the training process. Nonetheless, in contrast to the DropConnect technique, Dropout effectively improves the performance of VGG and AlexNet by a noticeable margin. Several

Performance for different BNNs								
model	Dropout		DropConnect		RT		Flipout	
metrics	VGG	Alex	VGG	Alex	VGG	Alex	VGG	Alex
MSE	0.05	0.1	0.45	0.68	0.08	0.30	0.04	0.05
NLL	-3.17	-1.39	-0.13	-0.08	-2.33	-2.01	-3.20	-3.62

TABLE II. Best performance described by MSE and NLL reached for Dropout, DropConnect, RT, and Flipout using both architectures over the test dataset.

works have shown that dropping weights (or neurons) does not bring much performance improvement in convolutional neural networks. Some authors attribute this failure to the incorrect placement in the convolutional blocks [101], while others assert that these methods fail in

some network architectures [48]. Since our aim is searching for a good BNN model useful to analyse the CMB dataset, hereafter, we will mostly focus on Dropout for both architectures. The analysis show that large values of Dropout rates are required to decrease the gap between training and validation, and dropping 10% of the neurons yields the highest performances. Conversely, besides producing better results with respect to AlexNet, VGG also reduces notably the training/validation gap, and only 1% of Dropout rate is required to score the best performance in the model (See Fig. 14 for AlexNet, and in Fig. 15 in Appendix B). We can ascribe this favorable behavior to batch renormalization which acts not only as a regularizer, but also avoids extra normalisation calculations during the forward pass that yield to a quick convergence. On the other hand, as discussed in Sec. VII, often neural networks are miscalibrated. We then estimate the coverage probabilities corresponding to confidence intervals of 68%, 95.5%, and 99.7% (i.e., 1σ , 2σ , and 3σ) in order to verify the accuracy of the uncertainty estimates. The results using AlexNet are shown in table III. We can notice that firstly as expected the coverage probability is proportional to the Dropout rate, since this variable is associated to the stochasticity of the model.

Coverage probability estimation for Dropout and DropConnect												
C.I	Rate		dr=1%		dr=5%		dr=7%		dr=10%		dr=20%	
	dO.	dC.	dO.	dC.	dO.	dC.	dO.	dC.	dO.	dC.	dO.	dC.
68.3%	52.1	54.9	65.0	66.5	68.3	68.3	73.1	68.4	77.1	76.2		
95.5%	84.2	88.2	93.8	96.0	95.0	97.0	97.2	98.1	98.4	99.1		
99.7%	96.3	96.9	99.3	99.8	99.4	99.6	99.8	99.8	99.9	99.9		

TABLE III. Estimation of coverage probabilities corresponding to confidence intervals of 1σ , 2σ , and 3σ . Dropout rate (dr) becomes a hyper parameter which should be tuned in order to calibrate the network. $Dr \sim 0.07$ and $dr \sim 0.05$ yield to accurate uncertainties for Dropout and DropConnect, respectively.

Epistemic and Aleatoric uncertainties										
Type of Uncertainty	Size		100%		80%		60%		40%	
	Drop	Flip	Drop	Flip	Drop	Flip	Drop	Flip	Drop	Flip
Epistemic	0.0024	0.0011	0.0028	0.0011	0.0033	0.0013	0.050	0.005		
Aleatoric	0.090	0.015	0.093	0.014	0.094	0.019	0.14	0.041		

TABLE IV. Aleatoric and epistemic uncertainties for a percent of the total training dataset sizes. The aleatoric uncertainty oscillates, while epistemic uncertainty decreases when training dataset gets larger. These results are compatible with those reported in [65]. There is an anomalous behavior for the 40% of the training subset, which can be explained with the significant overfitting of the model due to the small amount of data.

Interestingly, the Dropout rate that leads to the correct calibration is not necessarily equal to that one which yields to the best performance. This result supports the fact that calibration of deep neural networks after training becomes the most effective. Additionally, we observe that the Dropout rate used to calibrate DropConnect models is smaller than the one used in Dropout, suggesting

that a stronger stochasticity is involved in DropConnect networks (since there are more weights than neurons). The behavior in the VGG architecture is substantially different, we observe that is not possible to calibrate the network during training. Tuning the hyper parameters (Dropout rate or posterior regularization) is not enough to tune the uncertainties and thus calibrate the confidence intervals. This is due to the batch (re)normalization layers in the VGG architecture, the normalization applied at each layer indeed standardizes the activation (mean close to 0 and standard deviation close to 1), reducing or even nullifying the effect of the hyper parameters tuning on the epistemic uncertainties. Re-calibration after training must be applied in networks with batch (re)normalization layers. Therefore, an important result obtained so far is that calibrating networks during training is sometimes not enough, this necessarily depends on the architecture of the network, especially if the former contains transformation techniques on the weights like batch (re)normalization. We further computed the NLL for different trained dataset size (see Appendix C), finding a strong dependence on the amount of images used for training the network. We also computed the aleatoric and epistemic uncertainties for those experiments (see Table IV). Results show that reducing the training dataset size appreciable increases the epistemic uncertainty, while the aleatoric does not, as discussed in Sec. III. Thereby, observing the effect of the training dataset size on uncertainties should reflect the quality of the uncertainty measurement.

B. Reparameterization Trick and Flipout

In this section we evaluate the use of Flipout compared to RT on both architectures. The performance of both methods are shown in Table II. We have found that Flipout outperforms all other methods regardless the network architecture and also it has achieved significant speedups during the training process. As mentioned above, VGG tends to produce more miscalibrated networks. This effect was also observed using either Flipout or RT, while for AlexNet we have found out that calibration can be achieved by regularizing the scale parameter of the approximate posterior of the weights and biases. If the initially trained network is overestimating the error, we want to add a regularization reducing the variance of the approximate posterior. In the case in which the scale of the approximate posterior is parametrized with a softplus function, we can use a SUM regularizer on the parameters of the scale (before the softplus) to reduce the variance and an L2 regularizer to increase it (since the parameters of the scales are negative for a prior with scale around 1). We also changed the prior scale, but we have found this approach not effective. The amount of regularization on the parameters of the posterior scale thus play the role the hyper parameter required to calibrate the network.

In fact, regularizing the posterior allows to reduce the

Coverage probability estimation for Flipout and RT.												
C.I.	Reg		Non-Reg		Reg= $1e^{-7}$		Reg= $6e^{-6}$		Reg= $1e^{-5}$		Reg= $1e^{-4}$	
	Flip.	RT	Flip.	RT	Flip.	RT	Flip.	RT	Flip.	RT	Flip.	RT
	68.3%	63.3	66.3	65.1	66.5	68.2	67.6	70.0	68.1	89.6	70.0	
95.5%	91.9	94.6	92.9	94.8	95.2	95.2	95.9	95.5	99.4	95.9		
99.7%	98.8	99.4	98.9	99.4	99.4	99.6	99.7	99.6	100	99.6		

TABLE V. Estimation of coverage probabilities corresponding to the confidence intervals of 1σ , 2σ , and 3σ . The regularizer (Reg) becomes an hyper parameter which should be tuned in order to calibrate the network. $Reg = 6e^{-6}$ and $Reg = 1e^{-5}$ yield to roughly accurate uncertainties for Flipout and RT respectively. The bias used here is 0.001.

width of the posterior distribution, producing more accurate confidence estimates. A visualization of this effect can be seen in Appendix C. Table V reports the coverage probabilities corresponding to confidence intervals of 1σ , 2σ , and 3σ for different values of the regularization. We have found out that without any regularizer, the estimation of the error is permissive and enhancing this hyper parameter increases the coverage probability estimation until arriving at values very close to their corresponding confidence intervals. The values reached to calibrate the network are $\sim 6e^{-6}$ and $\sim 1e^{-5}$ for Flipout and RT, respectively. Fig. 16 in Appendix B displays the performance of the network for the models used in Table V only for Flipout. Despite the fact that BNNs incorporate some degree of regularization, the gap between training/validation still remains for AlexNet architecture, while for VGG it becomes small. Additionally, we can estimate both the epistemic and aleatoric uncertainties from the calibrated Flipout network. The results are shown in Table IV. As before, epistemic uncertainty increases with the size of the training dataset. However, we do observe that the epistemic uncertainties becomes smaller for Flipout compared to Dropout, implying that Flipout indeed achieves the largest variance reduction. The performance of the network using different training dataset sizes can be seen in Appendix C. Although the use of batch (re)normalization produces reduction on the training/validation gap, it also leads to large fluctuations due to the fact that it is constantly readjusting the layers to new distributions.

C. Approximated the Posterior Distribution of the Cosmological Parameters

So far we have analyzed the performance of different BNNs for each architecture. We have found out that Flipout and Dropout are methods which work really well to carry out parameter inference using our CMB dataset. After calibrating the network with the approach introduced in Sec. VII, we can visualize the performance of the above methods in terms of precision of their cosmological parameters predictions. Fig. 8 shows the correlation between the true parameters and the predicted parameters

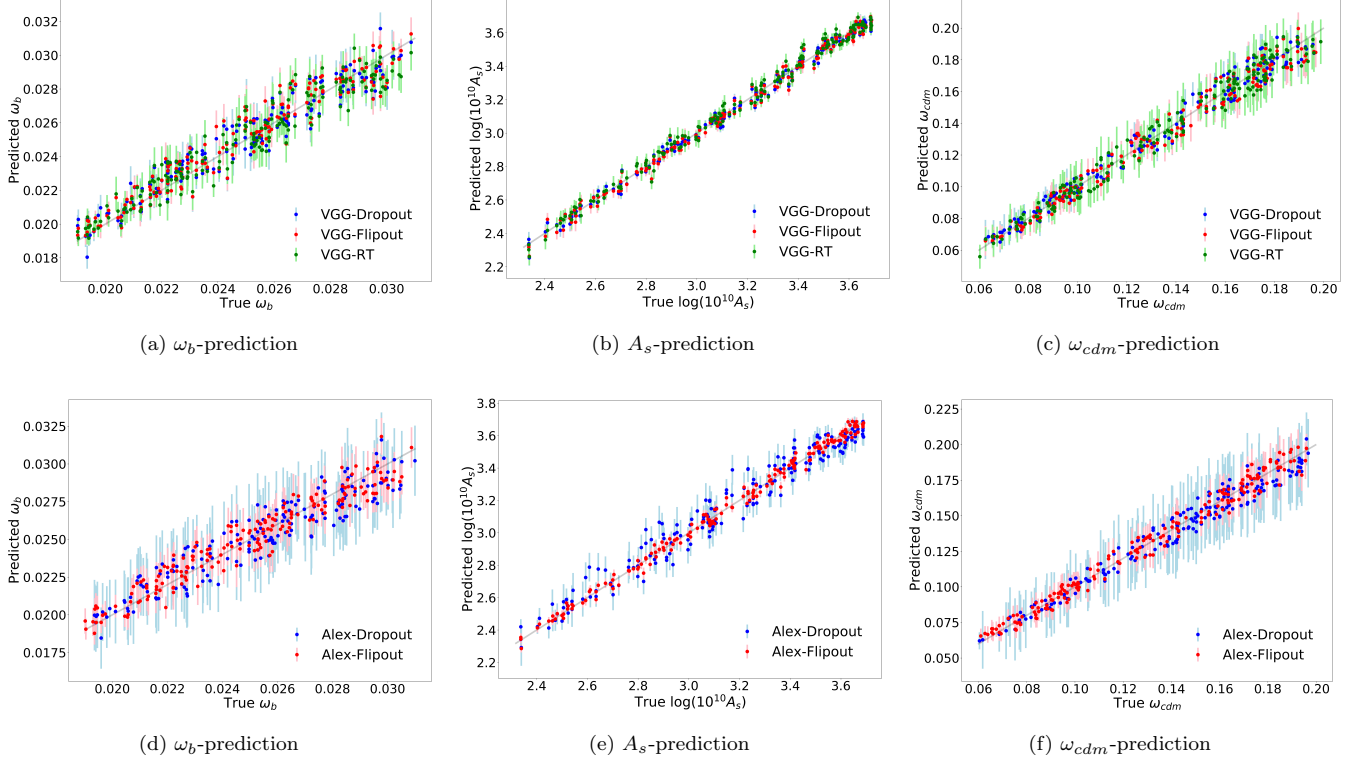


FIG. 8. Predictions of the BNN on the test dataset. Top and bottom panels show the results using VGG and AlexNet, respectively. Each panel shows the parameters used in the dataset and the values predicted from the CMB maps by the neural network. Dots mark the mean of the predictions for 2,500 samples in the test dataset, while the error bars represent their calibrated standard deviations. The colors display different BNNs along with the used architecture.

with the respective confidence intervals, on the test CMB maps. As mentioned in the previous section, implementing Dropout in the AlexNet architecture leads to large MSE values and larger uncertainties, while Flipout keeps excellent performance regardless the architecture, and its uncertainties are notably reduced. Finally, we constraint the dark-energy density written as $\Omega_\Lambda \approx 1 - \Omega_b - \Omega_{cdm}$, being $\omega_i \equiv \Omega_i h^2$ with $h = 0.6781$ [6], just to examine the posterior distribution for the derived parameters. The triangle plots of Figs. 9 and 19 show our main results for one example randomly picked from the CMB test dataset. We use the Python GetDist package for creating the triangular plot [98]. Fig. 9 displays the four most accurate BNNs which yield credible cosmological parameter contours. The target values for the selected example are $\omega_b = 0.02590$, $A_s = 3.65653$, $\omega_{cdm} = 0.15773$, the derived parameter $\Omega_\Lambda = 0.59761$, and in Table VI gives its marginalized parameter constraints from the CMB maps. In Appendix D we show the results for all the BNNs introduced in this paper.

Marginalized parameter constraints				
ACDM \ BNN	Flipout-Alex	Flipout-VGG	RT-VGG	Drop-VGG
ω_b	$0.0259^{+0.0021}_{-0.0021}$	$0.0259^{+0.0017}_{-0.0018}$	$0.0265^{+0.0016}_{-0.0016}$	$0.0258^{+0.0017}_{-0.0016}$
$\ln(10^{10} A_s)$	$3.659^{+0.048}_{-0.049}$	$3.650^{+0.057}_{-0.056}$	$3.669^{+0.059}_{-0.063}$	$3.655^{+0.046}_{-0.045}$
ω_{cdm}	$0.158^{+0.019}_{-0.019}$	$0.155^{+0.021}_{-0.021}$	$0.157^{+0.019}_{-0.019}$	$0.158^{+0.014}_{-0.015}$
Ω_Λ	$0.598^{+0.045}_{-0.043}$	$0.604^{+0.046}_{-0.047}$	$0.598^{+0.043}_{-0.042}$	$0.597^{+0.034}_{-0.032}$

TABLE VI. Parameters 95% intervals for the minimal base- Λ CDM model from our synthetic CMB dataset using Flipout, RT, and Dropout with the AlexNet and VGG architectures.

D. Parameter Estimation from Combination of Temperature and Polarization Maps

So far, we have obtained the parameter predictions only from maps of CMB temperature. Adding complementary information to the dataset such as a polarization, will provide better constraints on the cosmological model and also help to break some partial parameter degeneracies. In this subsection we present predictions of the parameters from the combinations of temperature and polarization which are significantly more precise than those determined using temperature alone. Cosmological experiments like Planck are designed to mea-

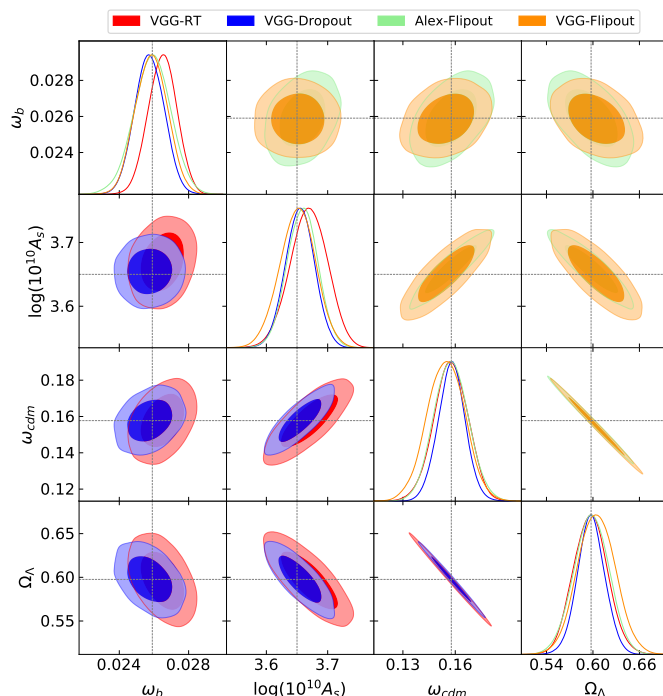


FIG. 9. Minimal base- Λ CDM 68% and 95% parameter constraint contours from one example of our synthetic CMB dataset using the best among four methods. The diagonal plots are the marginalized parameter constraints, the dashed lines stand for the predicted values and the black solid line corresponds to the true values $\omega_b = 0.02590$, $\log(10^{10} A_s) = 3.65653$ and $\omega_{cdm} = 0.15773$.

sure the Stokes parameters T , Q , U useful for analyzing the CMB radiation in terms of its temperature and polarization. This CMB radiation field can be expressed as a rank-2 tensor \mathcal{I}_{ij} , where $T = (\mathcal{I}_{11} + \mathcal{I}_{22})/4$ corresponds to the temperature anisotropy studied in the previous sections, while $Q = (\mathcal{I}_{11} - \mathcal{I}_{22})/4$ and $U = \mathcal{I}_{12}/2$ describe the linear polarization [102]. While T is a scalar invariant under rotations, Q and U depend on the reference frame determined by the direction of observation $\hat{\mathbf{n}}$ and two axes $(\hat{\mathbf{e}}_1, \hat{\mathbf{e}}_2)$ perpendicular to $\hat{\mathbf{n}}$. If $\hat{\mathbf{e}}_1$ and $\hat{\mathbf{e}}_2$ are rotated by an angle ψ , Q and U transform as [103]

$$(Q \pm iU)'(\hat{\mathbf{n}}) = e^{\mp 2i\psi} (Q \pm iU)(\hat{\mathbf{n}}), \quad (22)$$

where the prime denotes the quantities in the transformed coordinate system. For these objects, one can construct two real quantities usually called E and B which are invariant under rotations, but they behave differently under parity (E remains unchanged, while B changes sign) [104]. Therefore, adding polarization and assuming that CMB fluctuations are Gaussian, the statistical properties of the CMB in the sky are fully encoded in four power spectra C^{TT} , C^{EE} , C^{BB} , and C^{TE} .

In order to estimate the cosmological parameters directly from the CMB maps, we run again the script used in Sec. VI but this time, generating the four power spectra

with the CLASS code. Those spectra are given in input to healy which produces three maps associated for: T , Q , and U . Finally, these three maps are stacked in order to create images of size $256 \times 256 \times 3$, analogous to the RGB images, where each channel corresponds to a map measured by the cosmological experiment. We choose the Flipout method for estimating the cosmological parameters from temperature and polarization maps due to the notable performances found previously. We use the VGG architecture since yield the best results for the temperature map alone, and we calibrate the network after training with the usual method of Sec. VII. We made

Metrics for the Network with Polarization				
Metrics \ Size	100%	80%	60%	40%
Epistemic	$9.50e^{-5}$	$10.01e^{-5}$	$9.51e^{-5}$	$10.40e^{-5}$
Aleatoric	$1.2e^{-3}$	$1.3e^{-3}$	$1.2e^{-3}$	$1.9e^{-3}$
NLL	-5.932	-5.911	-5.897	-5.380
MSE	0.0034	0.0034	0.0036	0.0060
C.I-1 σ	68.6%	67.9%	67.1%	71.5%
C.I-2 σ	94.7%	94.7%	93.1%	94.6%
C.I-3 σ	98.8%	98.7%	98.9%	99.2%

TABLE VII. Assessment of Flipout model using synthetic CMB temperature and polarization maps. Below is reported the Confidence Interval results for 68%, 95.5% and 99.7%.

several experiment varying the size of the training set, the results are shown in Table VII. Despite of the results obtained in Table IV, we can observe how epistemic and aleatoric remains approximately constant. In this case, thanks to the additional information provided by the polarization channel, even the 40% percent of the data seems to be enough for training the network properly reaching convergence of the uncertainties. With respect to the temperature map alone, the values for both uncertainties decrease one order of magnitude and the gap between them is also reduced. Furthermore, the MSE decreases almost one order of magnitude with respect to the values found in Subsec. VIII C. The predictions for each cosmological parameter are displayed in Fig. 10. Evidently, we can observe the improvements provided by polarization, in particular the reduction of uncertainty intervals for all parameters. In order to show the parameter intervals and contours from the combined CMB and polarization map, we choose randomly an example from the test set with true values $\omega_b = 0.0201$, $\log(10^{10} A_s) = 3.6450$ and $\omega_{cdm} = 0.1736$. The two-dimensional posterior distribution of the cosmological parameters are shown in Fig. 11 and the parameter 95% intervals are given by

$$\begin{aligned} \omega_b &= 0.02015_{-0.00086}^{+0.00086}, & \log(10^{10} A_s) &= 3.680_{-0.052}^{+0.052} \\ \omega_{cdm} &= 0.178_{-0.016}^{+0.016}, & \Omega_\Lambda &= 0.565_{-0.037}^{+0.037} \end{aligned} \quad (23)$$

Comparing Figures 11 and 9 we can observe that adding polarization data provides considerably tighter constraints on all parameters than can be obtained from only temperature data. Presence of polarization information can break degeneracies among parameters

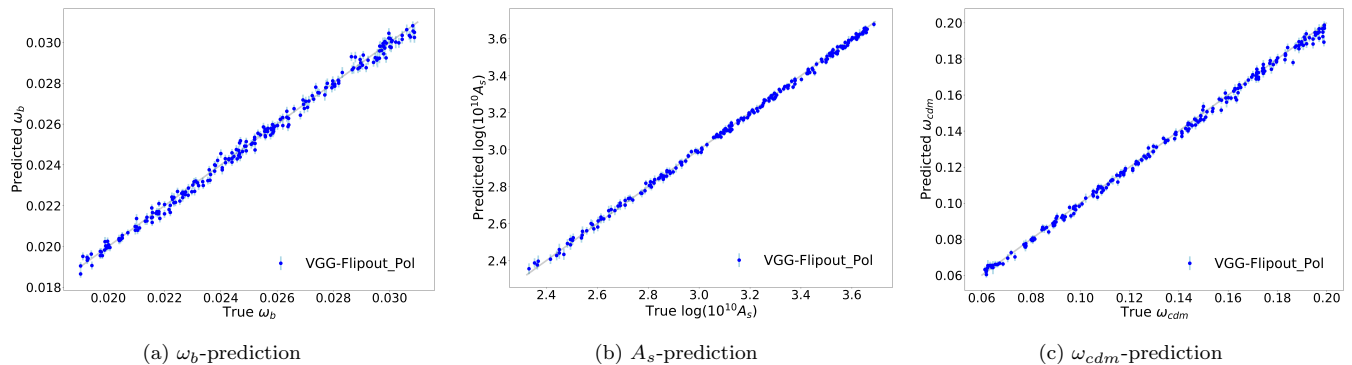


FIG. 10. Predictions of the BNN on the test dataset. The plots show the parameters used in the dataset and the values predicted from the CMB temperature plus polarization maps by the neural network. Dots mark the mean of the predictions for 2,500 samples in the test dataset, while the error bars represent their calibrated standard deviations. Here we use the Flipout method.

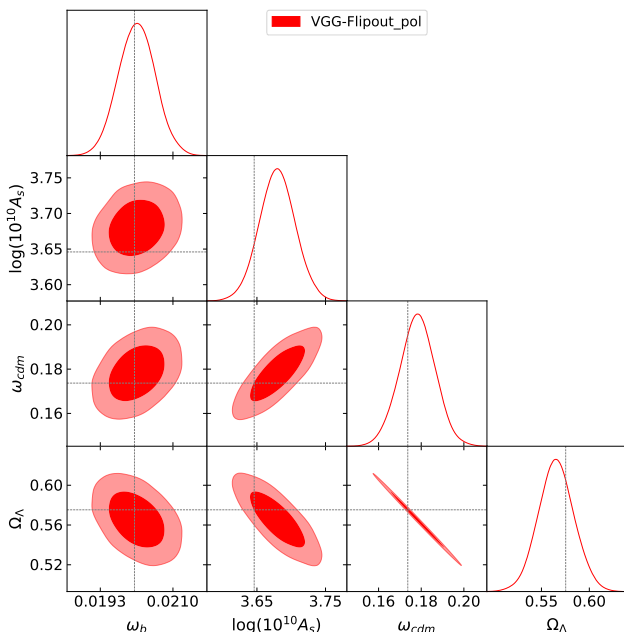


FIG. 11. Minimal base- Λ CDM 68% and 95% parameter constraint contours from one example of our synthetic CMB dataset with temperature and polarization using Flipout. The diagonal plots are the marginalized parameter constraints, the dashed lines stand for the predicted values and the black solid line corresponds to the true values.

and stringent its constraints which is consistent with our preliminary power spectrum analysis in Sec. II. The parameter degeneracy that determines the incapacity to distinguish certain parameter combinations, emerges not only from physical effects such as a geometrical degeneracy [105], but also from low numerical precision in the methods used for computing the cosmological observables [106]. In this case, the distinctive effects that

ω_b produces in temperature and polarization spectra allows the network to recognize the impact of this parameter in the maps.

E. Calibrating Bayesian Networks via Gradient Descent

Temperature Scaling (TS) is one of the most appealing method used in literature for calibration [107]. It consists in finding the value of a scalar parameter on validation set such that minimize NLL. We argue that this method can only reduce aleatoric uncertainties, while it cannot reduce epistemic uncertainties in BNNs driven by the means of the prediction distributions. To this aim, we propose a technique that re-adjust the weights in the last layer of the network which are associated to both means and covariance of the output distribution. We call Last Layer the method that affects all last layer, while we call Last Layer Loc the method affecting only the weights associated with the prediction means. The NLL function Eq. (19) can be transformed in two ways: $\Sigma \rightarrow s\Sigma$ being $s \in \mathbb{R}^+$ a scalar parameter, (which is the TS method) and $\Sigma \rightarrow L\Sigma L^T$ being L a lower triangle matrix. In order to verify the reliability of these methods, we load the weights computed from the model reported in Subsec. VIII D and we optimize the NLL for 100 epochs after convergence. The obtained results are reported in Table VIII. We can observe that for the last layers methods (LL and LL-loc) the NLL and MSE is reduced significantly with respect to the values found in Table VII (100% column), and the aleatoric uncertainty is also notably reduced for all methods.

Minimizing a scalar produce the same orientations that we found with the method used in the previous sections, while the use of lower triangular matrix as a scaling reorient a bit the ellipses during calibration. Unfortunately all methods seem to produce poor estimations for the confi-

Metrics for our calibrated methods						
Methods	LL_S	LL_T	$LL - loc_S$	$LL - loc_T$	TS_S	TS_T
Epistemic	$2.4e^{-4}$	$2.4e^{-4}$	$2.4e^{-4}$	$2.4e^{-4}$	$2.4e^{-4}$	$2.4e^{-4}$
Aleatoric	$9.6e^{-4}$	$9.7e^{-4}$	$9.6e^{-4}$	$9.2e^{-4}$	$12.3e^{-4}$	$11.1e^{-4}$
NLL	-6.71	-6.67	-6.31	-6.50	-6.06	-6.13
MSE	0.0026	0.0026	0.0027	0.0026	0.0033	0.0032
C.I- 1σ	79.1%	79.1%	80.0%	79.6%	79.0%	77.2%
C.I- 2σ	97.8%	97.8%	98.5%	98.0%	98.3%	97.7%
C.I- 3σ	99.9%	99.9%	99.9%	99.9%	99.9%	99.6%

TABLE VIII. Assessment of Flipout model using synthetic CMB temperature and polarization maps. In this case, the calibration was achieved using three proposal methods: Temperature Scaling (TS), Last Layer (LL) and Last Layer only with the mean (LL-loc). In each case, the temperature scaling parameters are either a single scalar (S) or a lower triangular matrix (T). We report also the Confidence Interval results for 1σ , 2σ and 3σ .

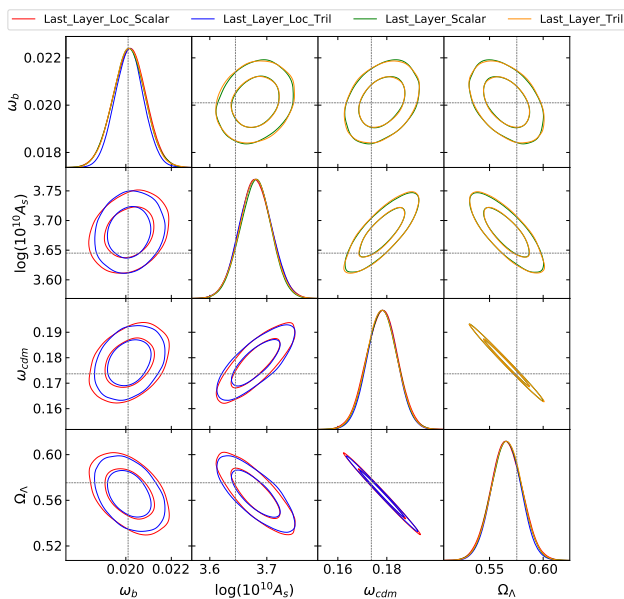


FIG. 12. Minimal base- Λ CDM 68% and 95% parameter constraint contours from one example of our synthetic CMB dataset using Flipout. In this case, the calibration was achieved using two proposal methods: Last Layer and Last Layer only with the mean(Loc). In each case, the optimizer parameter is either a scalar or a matrix (Tri).

dence intervals. However, preliminary results have shown that some techniques combined with TS leads to more reliable uncertainty estimates [108]. One of these techniques is related to the generalization of the KL-divergence used in VI, Eq. 5. Using approximate approaches such BB- α [109], we found that some divergences related to Hellinger distances or power Expectation Propagation (EP) method yield to well-calibrated networks. Fig. 12 shows the contours at 68% and 95% using the example shown in the previous subsection. Here we have used the combination of our proposal method with the BB-alpha

where its hyper-parameters were adapted to work with the power EP method. For all methods, there is no distinction between using temperature scaling scalar (S) or a lower triangular matrix (T) finding its consistently outputs with well-calibrated credible intervals. More detailed analysis about these calibration proposals will be the object of future works [108].

IX. CONCLUSIONS

We have employed Bayesian neural networks as a reliable and accurate tool to estimate the posterior distribution of the cosmological parameters directly from simulated CMB maps. BNNs, when properly trained and calibrated, offer the capability to estimate the total uncertainty (aleatoric and epistemic) of their predictions. They are trained by imposing a prior distribution on the parameters of the network (weights) and approximating the posterior distribution using Variational Inference. Different assumptions about the distribution over the weights have been proposed, and four of them were used in this work: Dropout, DropConnect, Flipout, and Reparameterization Trick. We have compared them by implementing two architectures and several calibration methods.

Takeaway messages:

1. As a proof-of-principle, we have compared Variational Inference (VI) and MCMC techniques finding that the latter excels at quantifying uncertainty, while the former is about 10000 times faster at inference. Using the covariance matrix efficiently estimated from the BNNs samples as initial proposal in MCMC, significantly increases the acceptance rate and gives faster convergence.
2. Flipout emerged as the most reliable and effective method, achieving best performances across architectures, while DropConnect had the worst performances. Furthermore, we observed that Flipout converges much faster during training and manifests a notable reduction in the credible contours for the parameters.
3. Calibrating after training becomes the best option. In fact, we showed that hyper parameter tuning in training is not sufficient in the cases where batch (re)normalization is present in the architecture. Therefore, calibration in these architectures is only possible after training. Using batch (re)normalization is advantageous since it allows us to obtain the best performances and the highest convergence rate during training while focusing on calibration after.
4. We observed that tuning the regularization parameter for the scale of the approximate posterior on

the weights in Flipout and RT we can produce unbiased and reliable uncertainty estimates, similar to Dropout rate in MCDropout.

5. Parametric methods for calibration introduced in Sec. VIII are simple but quite successful. Different calibration methods based on gradient descent have also been proposed, to be used alone or in combination with Temperature Scaling. Further investigation on these calibration methods will be the object of future studies.
6. In Subsec. VIII D we show how polarization can be combined with the temperature in a unique multi-channel input tensor, allowing the network to automatically extract complex information from partial sky coverage maps and significantly reducing the prediction errors (see Fig. 11 and Table VII). The outcomes of this subsection establish a remarkable result that will be further explored in subsequent studies.

The research showed in this paper allows to extract

relevant features directly from the raw data such as non-Gaussian signals [110] or foreground emissions [111, 112]. In future work, we plan to carry out this comparison improving the architecture and using other cosmological datasets such as large-scale matter distribution or 21cm maps. The data generator script and MCMC chains given here are available at [113]. The library Argo used for obtaining the results reported in this paper can be found at [114].

ACKNOWLEDGMENTS

H.J. Hortúa, R. Volpi, and L. Malagò are supported by the DeepRiemann project, co-funded by the European Regional Development Fund and the Romanian Government through the Competitiveness Operational Programme 2014-2020, Action 1.1.4, project ID P.37-714, contract no. 136/27.09.2016. D. Marinelli acknowledges the RIST institute where he was employed when this project started and the initial support from the DeepRiemann project.

-
- [1] M. Giovannini, *A Primer on the Physics of the Cosmic Microwave Background* (World Scientific, 2008).
 - [2] P. Naselsky, D. Novikov, and I. Novikov, *The Physics of the Cosmic Microwave Background*, Cambridge Astrophysics (Cambridge University Press, 2006).
 - [3] P. Collaboration, Planck 2015 results - xiii. cosmological parameters, *A&A* **594**, A13 (2016).
 - [4] M. Giovannini, Why CMB physics?, *Int. J. Mod. Phys. A* **22**, 2697 (2007), arXiv:astro-ph/0703730 [astro-ph].
 - [5] S. Dodelson and A. P. L. (1941-1969)., *Modern Cosmology* (Elsevier Science, 2003).
 - [6] P. Collaboration (Planck), Planck 2018 results. VI. Cosmological parameters, arXiv:1807.06209v1 (2018).
 - [7] P. Collaboration, Planck 2018 results. X. Constraints on inflation, arXiv e-prints, arXiv:1807.06211 (2018), arXiv:1807.06211 [astro-ph.CO].
 - [8] S. Mishra-Sharma, D. Alonso, and J. Dunkley, Neutrino masses and beyond- Λ CDM cosmology with lsst and future cmb experiments, *Phys. Rev. D* **97**, 123544 (2018).
 - [9] W. Deng, Dark energy constraints in light of pantheon sne ia, bao, cosmic chronometers and cmb polarization and lensing data, *Phys. Rev. D* **97**, 123507 (2018).
 - [10] C. Pitrou, A. Coc, J.-P. Uzan, and E. Vangioni, Precision big bang nucleosynthesis with improved helium-4 predictions, *Physics Reports* **754**, 1 (2018), precision big bang nucleosynthesis with improved Helium-4 predictions.
 - [11] H. J. Hortúa and L. Castañeda, Reduced bispectrum seeded by helical primordial magnetic fields, *Journal of Cosmology and Astroparticle Physics* **2017** (06), 020.
 - [12] M. Shiraishi, Probing the early universe with the cmb scalar, vector and tensor bispectrum, Springer Theses 10.1007/978-4-431-54180-6 (2013).
 - [13] <http://www.cfhtlens.org/>
<http://kids.strw.leidenuniv.nl/index.php>
<http://www.darkenergysurvey.org>
 - [14] <http://hsc.mtk.nao.ac.jp/ssp/>
<http://www.lsst.org>
<http://sci.esa.int/euclid/>
<http://wfirst.gsfc.nasa.gov>
<https://cmb-s4.org/>
<http://www.litebird-europe.eu/>
<http://www.core-mission.org/>
<https://simonsobservatory.org/>.
 - [15] <http://class-code.net>.
 - [16] D. Blas, J. Lesgourgues, and T. Tram, The cosmic linear anisotropy solving system (CLASS). part II: Approximation schemes, *Journal of Cosmology and Astroparticle Physics* **2011** (07), 034.
 - [17] J. Torrado and A. Lewis, Cobaya: Code for bayesian analysis of hierarchical physical models (2020), arXiv:2005.05290 [astro-ph.IM].
 - [18] <http://baudren.github.io/montepython.html>.
 - [19] R. Trotta, Bayes in the sky: Bayesian inference and model selection in cosmology, *Contemporary Physics* **49**, 71 (2008), <https://doi.org/10.1080/00107510802066753>.
 - [20] N. Kriegeskorte and T. Golan, Neural network models and deep learning - a primer for biologists, arXiv e-prints, arXiv:1902.04704 (2019), arXiv:1902.04704 [q-bio.NC].
 - [21] H. W. Lin, M. Tegmark, and D. Rolnick, Why does deep and cheap learning work so well?, *Journal of Statistical Physics* **168**, 1223 (2017).
 - [22] <https://github.com/marius311/pypico>.
 - [23] W. A. Fendt and B. D. Wandelt, Pico: Parameters for the Impatient Cosmologist, *Astrophys. J.* **654**, 2 (2006), arXiv:astro-ph/0606709 [astro-ph].
 - [24] J. Albers, C. Fidler, J. Lesgourgues, N. Schöneberg, and J. Torrado, CosmicNet I: Physics-driven implementation of neural networks within Boltzmann-Einstein solvers, arXiv e-prints, arXiv:1907.05764 (2019), arXiv:1907.05764 [astro-ph.CO].

- [24] A. Manrique-Yus and E. Sellentin, Euclid-era cosmology for everyone: Neural net assisted MCMC sampling for the joint 3x2 likelihood, arXiv e-prints , arXiv:1907.05881 (2019), [arXiv:1907.05881 \[astro-ph.CO\]](#).
- [25] F. Lanusse, Q. Ma, N. Li, T. E. Collett, C.-L. Li, S. Ravanbakhsh, R. Mandelbaum, and B. Poczcos, CMU DeepLens: deep learning for automatic image-based galaxy–galaxy strong lens finding, *Mon. Not. Roy. Astron. Soc.* **473**, 3895 (2018), [arXiv:1703.02642 \[astro-ph.IM\]](#).
- [26] C. E. Petrillo, C. Tortora, S. Chatterjee, G. Vernardos, L. V. E. Koopmans, G. Verdoes Kleijn, N. R. Napolitano, G. Covone, P. Schneider, A. Grado, and J. McFarland, Finding strong gravitational lenses in the Kilo Degree Survey with Convolutional Neural Networks, *mnras* **472**, 1129 (2017), [arXiv:1702.07675 \[astro-ph.GA\]](#).
- [27] J. Schmelzle, A. Lucchi, T. Kacprzak, A. Amara, R. Sgier, A. Réfrégier, and T. Hofmann, Cosmological model discrimination with Deep Learning, arXiv1707.05167 (2017).
- [28] N. Perraudin, M. Defferrard, T. Kacprzak, and R. Sgier, DeepSphere: Efficient spherical Convolutional Neural Network with HEALPix sampling for cosmological applications, *Astron. Comput.* **27**, 130 (2019), [arXiv:1810.12186 \[astro-ph.CO\]](#).
- [29] R. Ciuca, O. F. Hernáandez, and M. G. Wolman, A convolutional neural network for cosmic string detection in cmb temperature maps (2017).
- [30] Y. D. Hezaveh, L. Perreault Levasseur, and P. J. Marshall, Fast Automated Analysis of Strong Gravitational Lenses with Convolutional Neural Networks, *Nature* **548**, 555 (2017), [arXiv:1708.08842 \[astro-ph.IM\]](#).
- [31] L. Perreault Levasseur, Y. D. Hezaveh, and R. H. Wechsler, Uncertainties in Parameters Estimated with Neural Networks: Application to Strong Gravitational Lensing, *Astrophys. J.* **850**, L7 (2017), [arXiv:1708.08843 \[astro-ph.CO\]](#).
- [32] A. Gupta, J. M. Z. Matilla, D. Hsu, and Z. Haiman, Non-Gaussian information from weak lensing data via deep learning, *Phys. Rev.* **D97**, 103515 (2018), [arXiv:1802.01212 \[astro-ph.CO\]](#).
- [33] D. Ribli, B. Ármin Pataki, J. M. Zorrilla Matilla, D. Hsu, Z. Haiman, and I. Csabai, Weak lensing cosmology with convolutional neural networks on noisy data, arXiv e-prints , arXiv:1902.03663 (2019), [arXiv:1902.03663 \[astro-ph.CO\]](#).
- [34] J. Fluri, T. Kacprzak, A. Refregier, A. Amara, A. Lucchi, and T. Hofmann, Cosmological constraints from noisy convergence maps through deep learning, *Phys. Rev.* **D98**, 123518 (2018), [arXiv:1807.08732 \[astro-ph.CO\]](#).
- [35] A. Doussot, E. Eames, and B. Semelin, Improved supervised learning methods for EoR parameters reconstruction, arXiv e-prints , arXiv:1904.04106 (2019), [arXiv:1904.04106 \[astro-ph.CO\]](#).
- [36] N. Gillet, A. Mesinger, B. Greig, A. Liu, and G. Ucci, Deep learning from 21-cm tomography of the cosmic dawn and reionization, *mnras* **484**, 282 (2019), [arXiv:1805.02699 \[astro-ph.CO\]](#).
- [37] S. He, S. Ravanbakhsh, and S. Ho, [Analysis of cosmic microwave background with deep learning](#) (2018).
- [38] J. Caldeira, W. Wu, B. Nord, C. Avestruz, S. Trivedi, and K. Story, Deepcmb: Lensing reconstruction of the cosmic microwave background with deep neural networks, *Astronomy and Computing* **28**, 100307 (2019).
- [39] N. Krachmalnicoff and M. Tomasi, Convolutional Neural Networks on the HEALPix sphere: a pixel-based algorithm and its application to CMB data analysis, *A&A* **628**, A129 (2019), [arXiv:1902.04083 \[astro-ph.IM\]](#).
- [40] H. U. Norgaard-Nielsen, Excess b-modes extracted from the planck polarization maps, *Astronomische Nachrichten* **337**, 662 (2016).
- [41] S. He, Y. Li, Y. Feng, S. Ho, S. Ravanbakhsh, W. Chen, and B. Poczcos, Learning to predict the cosmological structure formation, *Proceedings of the National Academy of Sciences* **116**, 13825 (2019).
- [42] Y. Kwon, J.-H. Won, B. J. Kim, and M. C. Paik, Uncertainty quantification using bayesian neural networks in classification: Application to biomedical image segmentation, *Computational Statistics and Data Analysis* **142**, 106816 (2020).
- [43] G. Pereyra, G. Tucker, J. Chorowski, L. Kaiser, and G. E. Hinton, Regularizing neural networks by penalizing confident output distributions, *CoRR abs/1701.06548* (2017), [arXiv:1701.06548](#).
- [44] Y. Gal and Z. Ghahramani, Dropout as a Bayesian approximation: Insights and applications, in *Deep Learning Workshop, ICML* (2015).
- [45] N. Srivastava, G. Hinton, A. Krizhevsky, I. Sutskever, and R. Salakhutdinov, Dropout: A simple way to prevent neural networks from overfitting, *Journal of Machine Learning Research* **15**, 1929 (2014).
- [46] W. R. Morningstar, Y. D. Hezaveh, L. Perreault Levasseur, R. D. Blandford, P. J. Marshall, P. Putzky, and R. H. Wechsler, Analyzing interferometric observations of strong gravitational lenses with recurrent and convolutional neural networks, arXiv e-prints , arXiv:1808.00011 (2018), [arXiv:1808.00011 \[astro-ph.IM\]](#).
- [47] Y. Wen, P. Vicol, J. Ba, D. Tran, and R. Grosse, Flipout: Efficient pseudo-independent weight perturbations on mini-batches, in *International Conference on Learning Representations* (2018).
- [48] Y. Gal and Z. Ghahramani, Bayesian convolutional neural networks with bernoulli approximate variational inference (2015), [arXiv:1506.02158 \[stat.ML\]](#).
- [49] I. Osband, J. Aslanides, and A. Cassirer, Randomized Prior Functions for Deep Reinforcement Learning, arXiv e-prints , arXiv:1806.03335 (2018), [arXiv:1806.03335 \[stat.ML\]](#).
- [50] C. Guo, G. Pleiss, Y. Sun, and K. Q. Weinberger, On calibration of modern neural networks, in *Proceedings of the 34th International Conference on Machine Learning - Volume 70*, ICML'17 (JMLR.org, 2017) pp. 1321–1330.
- [51] A. Graves, Practical variational inference for neural networks, in *Advances in Neural Information Processing Systems 24*, edited by J. Shawe-Taylor, R. S. Zemel, P. L. Bartlett, F. Pereira, and K. Q. Weinberger (Curran Associates, Inc., 2011) pp. 2348–2356.
- [52] N. Metropolis, A. W. Rosenbluth, M. N. Rosenbluth, A. H. Teller, and E. Teller, Equation of state calculations by fast computing machines, *The Journal of Chemical Physics* **21**, 1087 (1953), <https://doi.org/10.1063/1.1699114>.
- [53] J. Regier, A. C. Miller, D. Schlegel, R. P. Adams, J. D. McAuliffe, and Prabhat, Approximate inference for constructing astronomical catalogs from images (2018), [arXiv:1803.00113 \[stat.AP\]](#).
- [54] A. Jain, P. K. Srijith, and S. Desai, Variational inference

- as an alternative to mcmc for parameter estimation and model selection (2018), [arXiv:1803.06473](https://arxiv.org/abs/1803.06473) [[astro-ph.IM](#)].
- [55] L. Verde, A practical guide to basic statistical techniques for data analysis in cosmology (2007), [arXiv:0712.3028](https://arxiv.org/abs/0712.3028) [[astro-ph](#)].
- [56] A. Lewis, Efficient sampling of fast and slow cosmological parameters, *Phys. Rev. D* **87**, 103529 (2013).
- [57] J. Dunkley, M. Bucher, P. G. Ferreira, K. Moodley, and C. Skordis, Fast and reliable Markov chain Monte Carlo technique for cosmological parameter estimation, *Monthly Notices of the Royal Astronomical Society* **356**, 925 (2005), <https://academic.oup.com/mnras/article-pdf/356/3/925/3140829/356-3-925.pdf>.
- [58] A. Zonca, L. Singer, D. Lenz, M. Reinecke, C. Rosset, E. Hivon, and K. Gorski, healpy: equal area pixelization and spherical harmonics transforms for data on the sphere in python, *Journal of Open Source Software* **4**, 1298 (2019).
- [59] A. Petri, Mocking the weak lensing universe: The LensTools Python computing package, *Astronomy and Computing* **17**, 73 (2016), [arXiv:1606.01903](https://arxiv.org/abs/1606.01903).
- [60] We run all single MCMC experiments in a CPU Intel Core i7-3840QM with clock speed of 2.80GHz, while the BNN was trained in a GPU: GeForce GTX 1080 Ti.
- [61] T. Salimans, D. P. Kingma, and M. Welling, Markov chain monte carlo and variational inference: Bridging the gap, in *Proceedings of the 32nd International Conference on International Conference on Machine Learning - Volume 37*, ICML'15 (JMLR.org, 2015) p. 1218–1226.
- [62] A. Thin, N. Kotelevskii, J.-S. Denain, L. Grinsztajn, A. Durmus, M. Panov, and E. Moulines, Metflow: A new efficient method for bridging the gap between markov chain monte carlo and variational inference (2020), [arXiv:2002.12253](https://arxiv.org/abs/2002.12253) [[stat.ML](#)].
- [63] G. O. Roberts, A. Gelman, and W. R. Gilks, Weak convergence and optimal scaling of random walk metropolis algorithms, *Ann. Appl. Probab.* **7**, 110 (1997).
- [64] A. D. Kiureghian and O. Ditlevsen, Aleatory or epistemic? does it matter?, *Structural Safety* **31**, 105 (2009), risk Acceptance and Risk Communication.
- [65] Y. Gal, *Uncertainty in Deep Learning*, Ph.D. thesis, University of Cambridge (2016).
- [66] N. Tagasovska and D. Lopez-Paz, Single-model uncertainties for deep learning (2018), [arXiv:1811.00908](https://arxiv.org/abs/1811.00908) [[stat.ML](#)].
- [67] G. Wang, W. Li, M. Aertsen, J. Deprest, S. Ourselin, and T. Vercauteren, Aleatoric uncertainty estimation with test-time augmentation for medical image segmentation with convolutional neural networks, *Neurocomputing* **338**, 34 (2019).
- [68] J. Fluri, T. Kacprzak, A. Lucchi, A. Refregier, A. Amara, T. Hofmann, and A. Schneider, Cosmological constraints with deep learning from kids-450 weak lensing maps, *Phys. Rev. D* **100**, 063514 (2019).
- [69] B. Lakshminarayanan, A. Pritzel, and C. Blundell, Simple and scalable predictive uncertainty estimation using deep ensembles (2016), [arXiv:1612.01474](https://arxiv.org/abs/1612.01474) [[stat.ML](#)].
- [70] Y. Kwon, J.-H. Won, B. Joon Kim, and M. Paik, International conference on medical imaging with deep learning , 13 (2018).
- [71] F. Laumann, K. Shridhar, and A. L. Maurin, Bayesian convolutional neural networks, (2018), [arXiv:1806.05978](https://arxiv.org/abs/1806.05978).
- [72] K. Shridhar, F. Laumann, and M. Liwicki, Uncertainty Estimations by Softplus normalization in Bayesian Convolutional Neural Networks with Variational Inference, arXiv e-prints , [arXiv:1806.05978](https://arxiv.org/abs/1806.05978) (2018), [arXiv:1806.05978](https://arxiv.org/abs/1806.05978) [[cs.LG](#)].
- [73] A. Kendall and Y. Gal, What uncertainties do we need in bayesian deep learning for computer vision? (2017), [arXiv:1703.04977](https://arxiv.org/abs/1703.04977) [[cs.CV](#)].
- [74] A. D. Cobb, M. D. Himes, F. Soboczenski, S. Zorzan, M. D. O’Beirne, A. G. Baydin, Y. Gal, S. D. Domagal-Goldman, G. N. Arney, and D. A. and, An ensemble of bayesian neural networks for exoplanetary atmospheric retrieval, *The Astronomical Journal* **158**, 33 (2019).
- [75] G. Dorta, S. Vicente, L. Agapito, N. D. F. Campbell, and I. Simpson, Structured uncertainty prediction networks, 2018 IEEE/CVF Conference on Computer Vision and Pattern Recognition [10.1109/cvpr.2018.00574](https://arxiv.org/abs/10.1109/cvpr.2018.00574) (2018).
- [76] Y. Gal and Z. Ghahramani, Dropout as a bayesian approximation: Representing model uncertainty in deep learning, in *Proceedings of The 33rd International Conference on Machine Learning*, Proceedings of Machine Learning Research, Vol. 48, edited by M. F. Balcan and K. Q. Weinberger (PMLR, New York, New York, USA, 2016) pp. 1050–1059.
- [77] Y. Gal and Z. Ghahramani, Bayesian convolutional neural networks with Bernoulli Approximate Variational Inference, in *4th International Conference on Learning Representations (ICLR) workshop track* (2016).
- [78] L. Wan, M. Zeiler, S. Zhang, Y. L. Cun, and R. Fergus, Regularization of neural networks using dropconnect, in *Proceedings of the 30th International Conference on Machine Learning*, Proceedings of Machine Learning Research, Vol. 28, edited by S. Dasgupta and D. McAllester (PMLR, Atlanta, Georgia, USA, 2013) pp. 1058–1066.
- [79] M. Aryan, N. H. V., M. Supratik, G. Naveen, and W. C. C., Dropconnect is effective in modeling uncertainty of bayesian deep networks, arXiv e-prints , [arXiv:1906.04569](https://arxiv.org/abs/1906.04569) (2019), [arXiv:1906.04569](https://arxiv.org/abs/1906.04569) [[cs.LG](#)].
- [80] P. McClure and N. Kriegeskorte, Robustly representing uncertainty in deep neural networks through sampling, (2016), [arXiv:1611.01639](https://arxiv.org/abs/1611.01639) [[cs.LG](#)].
- [81] K. D. P. and W. Max, Auto-encoding variational bayes, arXiv e-prints , [arXiv:1312.6114](https://arxiv.org/abs/1312.6114) (2013), [arXiv:1312.6114](https://arxiv.org/abs/1312.6114) [[stat.ML](#)].
- [82] D. P. Kingma, T. Salimans, and M. Welling, Variational Dropout and the Local Reparameterization Trick, arXiv e-prints , [arXiv:1506.02557](https://arxiv.org/abs/1506.02557) (2015), [arXiv:1506.02557](https://arxiv.org/abs/1506.02557) [[stat.ML](#)].
- [83] W. J. T, M. Riccardo, H. Frank, and D. M. Peter, The reparameterization trick for acquisition functions, arXiv e-prints , [arXiv:1712.00424](https://arxiv.org/abs/1712.00424) (2017), [arXiv:1712.00424](https://arxiv.org/abs/1712.00424) [[stat.ML](#)].
- [84] <https://www.tensorflow.org/>.
- [85] <https://www.tensorflow.org/probability>.
- [86] <https://sonnet.readthedocs.io/en/latest/>.
- [87] S. Liu and W. Deng, Very deep convolutional neural network based image classification using small training sample size, in *2015 3rd IAPR Asian Conference on Pattern Recognition (ACPR)* (2015) pp. 730–734.
- [88] A. Krizhevsky, I. Sutskever, and G. E. Hinton, Imagenet classification with deep convolutional neural networks, in *Proceedings of the 25th International Conference on Neural Information Processing Systems - Volume 1*, NIPS’12 (Curran Associates Inc., USA, 2012) pp. 1097–1105.
- [89] S. Ioffe, Batch renormalization: Towards reducing mini-

- batch dependence in batch-normalized models, in *NIPS* (2017).
- [90] D. P. Kingma and J. Ba, Adam: A Method for Stochastic Optimization, arXiv e-prints , arXiv:1412.6980 (2014), [arXiv:1412.6980 \[cs.LG\]](#).
- [91] Y. Ovadia, E. Fertig, J. Ren, Z. Nado, D. Sculley, S. Nowozin, J. V. Dillon, B. Lakshminarayanan, and J. Snoek, Can You Trust Your Model’s Uncertainty? Evaluating Predictive Uncertainty Under Dataset Shift, arXiv e-prints , arXiv:1906.02530 (2019), [arXiv:1906.02530 \[stat.ML\]](#).
- [92] M. Kull, T. S. Filho, and P. Flach, Beta calibration: a well-founded and easily implemented improvement on logistic calibration for binary classifiers, in *Proceedings of the 20th International Conference on Artificial Intelligence and Statistics*, Proceedings of Machine Learning Research, Vol. 54, edited by A. Singh and J. Zhu (PMLR, Fort Lauderdale, FL, USA, 2017) pp. 623–631.
- [93] Y. Gal, J. Hron, and A. Kendall, Concrete Dropout, arXiv e-prints , arXiv:1705.07832 (2017), [arXiv:1705.07832 \[stat.ML\]](#).
- [94] B. Zadrozny and C. Elkan, Obtaining calibrated probability estimates from decision trees and naive bayesian classifiers, in *Proceedings of the Eighteenth International Conference on Machine Learning*, ICML ’01 (Morgan Kaufmann Publishers Inc., San Francisco, CA, USA, 2001) pp. 609–616.
- [95] B. Zadrozny and C. Elkan, Transforming classifier scores into accurate multiclass probability estimates, in *Proceedings of the Eighth ACM SIGKDD International Conference on Knowledge Discovery and Data Mining*, KDD ’02 (ACM, New York, NY, USA, 2002) pp. 694–699.
- [96] J. C. Platt, Probabilistic outputs for support vector machines and comparisons to regularized likelihood methods, in *ADVANCES IN LARGE MARGIN CLASSIFIERS* (MIT Press, 1999) pp. 61–74.
- [97] V. Kuleshov, N. Fenner, and S. Ermon, Accurate Uncertainties for Deep Learning Using Calibrated Regression, arXiv e-prints , arXiv:1807.00263 (2018), [arXiv:1807.00263 \[cs.LG\]](#).
- [98] A. Lewis, Getdist: a python package for analysing monte carlo samples (2019), [arXiv:1910.13970 \[astro-ph.IM\]](#).
- [99] J. Sanchez, Mardia, k. v., j. t. kent, j. m. bibby: Multivariate analysis, *Biometrical Journal* **24**, 502 (1982).
- [100] H. Hotelling, The generalization of student’s ratio, *Ann. Math. Statist.* **2**, 360 (1931).
- [101] S. Cai, J. Gao, M. Zhang, W. Wang, G. Chen, and B. C. Ooi, Effective and efficient dropout for deep convolutional neural networks, *CoRR abs/1904.03392* (2019), [arXiv:1904.03392](#).
- [102] M. Zaldarriaga, Cosmic microwave background polarization experiments, *The Astrophysical Journal* **503**, 1 (1998).
- [103] M. Zaldarriaga, The polarization of the cosmic microwave background (2003), [arXiv:astro-ph/0305272 \[astro-ph\]](#).
- [104] J. Kaplan, J. Delabrouille, P. Fosalba, and C. Rosset, Cmb polarization as complementary information to anisotropies, *Comptes Rendus Physique* **4**, 917 (2003), dossier: The Cosmic Microwave Background.
- [105] G. Efstathiou and J. R. Bond, Cosmic confusion: degeneracies among cosmological parameters derived from measurements of microwave background anisotropies, *Monthly Notices of the Royal Astronomical Society* **304**, 75 (1999).
- [106] C. Howlett, A. Lewis, A. Hall, and A. Challinor, CMB power spectrum parameter degeneracies in the era of precision cosmology, *Journal of Cosmology and Astroparticle Physics* **2012** (04), 027.
- [107] D. Levi, L. Gispan, N. Giladi, and E. Fetaya, Evaluating and Calibrating Uncertainty Prediction in Regression Tasks, arXiv e-prints , arXiv:1905.11659 (2019), [arXiv:1905.11659 \[cs.LG\]](#).
- [108] H. J. Hortua, L. Malago, and R. Volpi, Reliable uncertainties for bayesian neural networks using alpha-divergences, in *Uncertainty and Robustness in Deep Learning Workshop, ICML* (2020).
- [109] J. M. Hernandez-Lobato, Y. Li, M. Rowland, D. Hernandez-Lobato, T. Bui, and R. E. Turner, Black-box alpha-divergence minimization (2015), [arXiv:1511.03243 \[stat.ML\]](#).
- [110] C. P. Novaes, A. Bernui, I. S. Ferreira, and C. A. Wuensche, A neural-network based estimator to search for primordial non-Gaussianity in Planck CMB maps, *jcnp* **2015**, 064 (2015), [arXiv:1409.3876 \[astro-ph.CO\]](#).
- [111] H. U. Nørgaard-Nielsen, Foreground removal from wmap 5yr temperature maps using an mlp neural network (2010).
- [112] H. U. Nørgaard-Nielsen, Confirmation of the detection of b modes in the planck polarization maps, *Astronomische Nachrichten* **339**, 432 (2018).
- [113] https://github.com/JavierOrjuela/BayesianNeuralNets_CMB.
- [114] <https://github.com/rist-ro/argo>.
- [115] N. Perraudin, M. Defferrard, T. Kacprzak, and R. Sgier, DeepSphere: Efficient spherical convolutional neural network with healpix sampling for cosmological applications, *Astronomy and Computing* **27**, 130 (2019).
- [116] A. Mathuriya, D. Bard, P. Mendygral, L. Meadows, J. Arnemann, L. Shao, S. He, T. Karna, D. Moise, S. J. Pennycook, K. Maschoff, J. Sewall, N. Kumar, S. Ho, M. Ringenburg, Prabhat, and V. Lee, CosmoFlow: Using Deep Learning to Learn the Universe at Scale, arXiv e-prints , arXiv:1808.04728 (2018), [arXiv:1808.04728 \[astro-ph.CO\]](#).
- [117] P. Graff, F. Feroz, M. P. Hobson, and A. Lasenby, BAMBİ: blind accelerated multimodal Bayesian inference, *mnras* **421**, 169 (2012), [arXiv:1110.2997 \[astro-ph.IM\]](#).
- [118] B. Phan, R. Salay, K. Czarnecki, V. Abdelzad, T. Denouden, and S. Vernekar, Calibrating Uncertainties in Object Localization Task, arXiv e-prints , arXiv:1811.11210 (2018), [arXiv:1811.11210 \[cs.LG\]](#).
- [119] A. D. Cobb, S. J. Roberts, and Y. Gal, Loss-Calibrated Approximate Inference in Bayesian Neural Networks, arXiv e-prints , arXiv:1805.03901 (2018), [arXiv:1805.03901 \[stat.ML\]](#).
- [120] D. Hendrycks, K. Lee, and M. Mazeika, Using pre-training can improve model robustness and uncertainty, *CoRR abs/1901.09960* (2019), [arXiv:1901.09960](#).
- [121] D. Hendrycks, K. Lee, and M. Mazeika, Using pre-training can improve model robustness and uncertainty, in *Proceedings of the 36th International Conference on Machine Learning*, Proceedings of Machine Learning Research, Vol. 97, edited by K. Chaudhuri and R. Salakhutdinov (PMLR, Long Beach, California, USA, 2019) pp. 2712–2721, [arXiv:1901.09960 \[cs.LG\]](#).
- [122] H. Song, T. Diethe, M. Kull, and P. Flach, Dis-

Appendix A: Evaluation of coverage probabilities through binned samples

As mentioned in Sec. VI, if the distribution that describes the samples drawn from the posterior is Gaussian, we can compute the coverage probabilities from the ellipsoidal confidence. However, this distribution sometimes

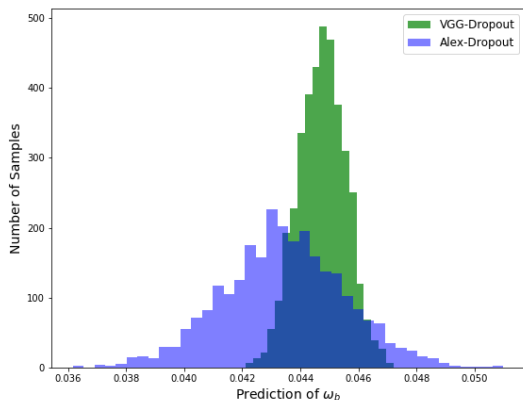


FIG. 13. Histogram generated from binned samples drawn from the posterior of the parameter ω_b using Dropout with the VGG (green) and AlexNet (blue) architectures. The mode for Dropout with VGG is 0.04478 while for the one with AlexNet is 0.04349. The true value is $\omega_b = 0.04492$.

		coverage probabilities from a binned samples					
C.I	Model	VGG-Dropout			Alex-Dropout		
		ω_b	A_s	ω_{cdm}	ω_b	A_s	ω_{cdm}
68.3%		68.1	67.1	63.3	68.5	67.1	66.7
95.5%		95.1	94.5	93.6	95.7	95.7	95.2
99.7%		99.6	99.5	98.9	99.8	99.6	99.4

TABLE IX. Estimation of coverage probabilities corresponding to confidence intervals of 1σ , 2σ and 3σ . AlexNet was trained with 7% dropout rate, while for VGG we used the network calibrated after training.

is not restricted to be Gaussian, especially for Dropout. In this case, we can follow the method used in [31] and generate a histogram from binned samples drawn from the posterior. Since this histogram is expected to be unimodal, we can compute the interval that contains the $(100\alpha)\%$ of the samples around the mode, with $\alpha \in [0, 1]$. Fig. 13 shows the histogram for ω_b where we can observe the difference by using both architectures, while Table IX reports the coverage probability for individual parameters. We can observe that the values are consistent with the ones expected for a calibrated network.

Appendix B: BNNs Hyper-parameters on the training process

Now, to understand the impact of the Dropout rate on the training process, we plot the NLL for different values of the parameter in Fig. 14 for AlexNet, and Fig. 15 for VGG, while Fig. 16 shows the results for AlexNet with Flipout being the regularized the hyper-parameter tuned during training.

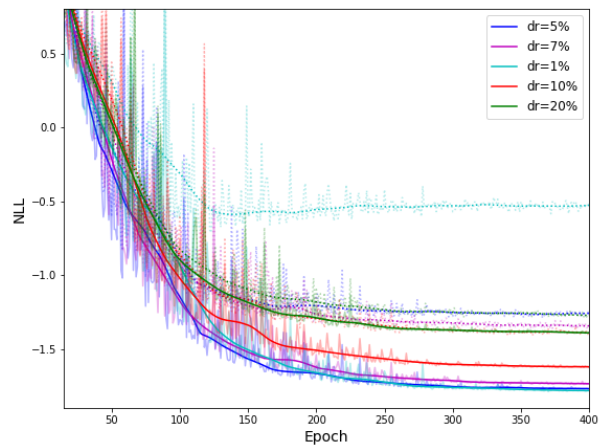


FIG. 14. Training (solid lines) and validation (dotted lines) for AlexNet. Negative log-likelihood for Dropout as a function of the epoch. The colors stand for the used Dropout rate (dr).

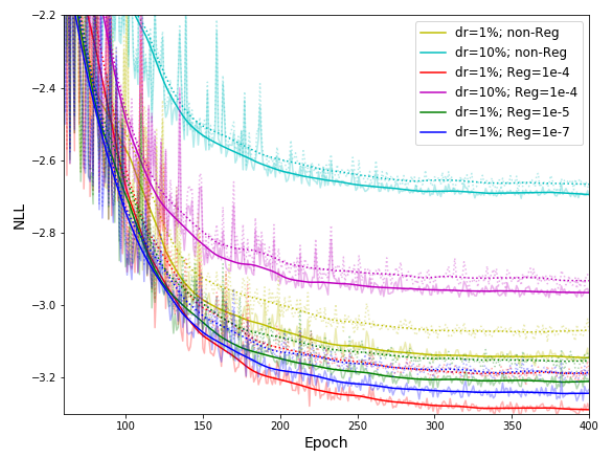


FIG. 15. Training (solid lines) and validation (dotted lines) Negative log-likelihood for dropout method as a function of epochs. The colors stand for the used dropout rate (dr). The VGG architecture was used for this case.

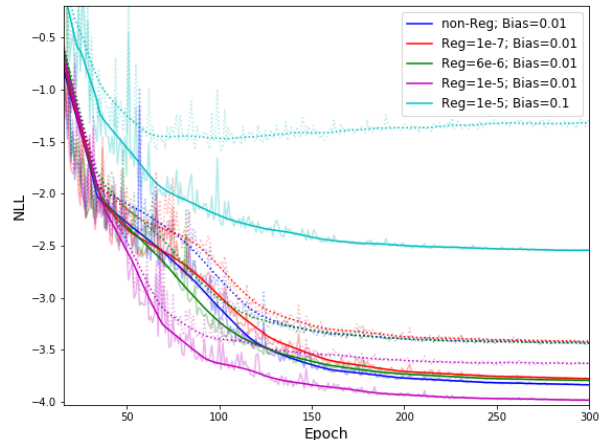


FIG. 16. *Training (solid lines) and validation (dotted lines) for AlexNet. Negative log-likelihood for Flipout method as a function of the epoch. The colors correspond to different regularizers and bias used.*

Appendix C: Performance of the BNN using different training dataset sizes

In this Appendix we show how the NLL is modified with respect to the training dataset sizes. This kind of

analysis not only presents the minimal training dataset size used for obtaining good performance, but also to claim that epistemic uncertainty can be reduced with sufficient training data [44]. Fig. 17 and Fig. 9 describe the Negative log-likelihood behavior for Dropout and Flipout respectively.

Appendix D: Triangle plots for CMB maps from different BNNs methods

Fig. 19 displays the results for all BNNs methods introduced in this paper. We can observe that the AlexNet architecture does not work well for RT and Dropout, while for RT we obtained low performance with respect to Flipout and Dropout. In Table X we report the marginalized parameter constraints from the CMB maps. What we can conclude from these results is that the performance for both RT and Dropout depends strongly of the architecture used, as was reported in [48], while for Flipout we do not find this issue. Therefore, Flipout is a more flexible and robust method for obtaining uncertainties at least for CMB dataset.

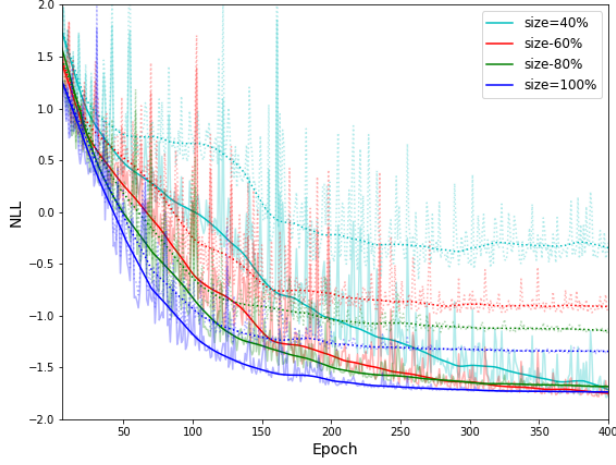


FIG. 17. Training (solid lines) and validation (dotted lines) for AlexNet. Negative log-likelihood for Dropout method as a function of the epoch. The colors represent the training dataset size used for a dropout rate of $dr = 0.07$.

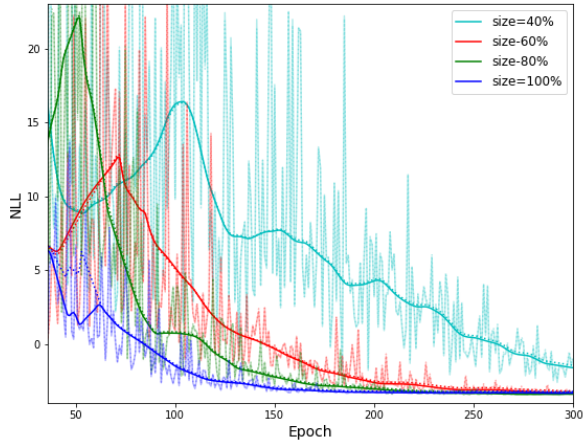


FIG. 18. Training (solid lines) and validation (dotted lines) for VGG. Negative log-likelihood for Flipout method as a function of the epoch. The colors correspond to different training dataset size.

Marginalized parameter constraints		
Λ CDM \ BNN	Drop-Alex	RT-Alex
ω_b	$0.0245^{+0.0040}_{-0.0039}$	$0.0237^{+0.0065}_{-0.0064}$
$\ln(10^{10} A_s)$	$3.59^{+0.12}_{-0.14}$	$3.633^{+0.088}_{-0.093}$
ω_{cdm}	$0.137^{+0.038}_{-0.038}$	$0.146^{+0.036}_{-0.037}$

TABLE X. Parameter 95% intervals for the minimal base- Λ CDM model from our synthetic CMB dataset using RT and Dropout with Alexnet.

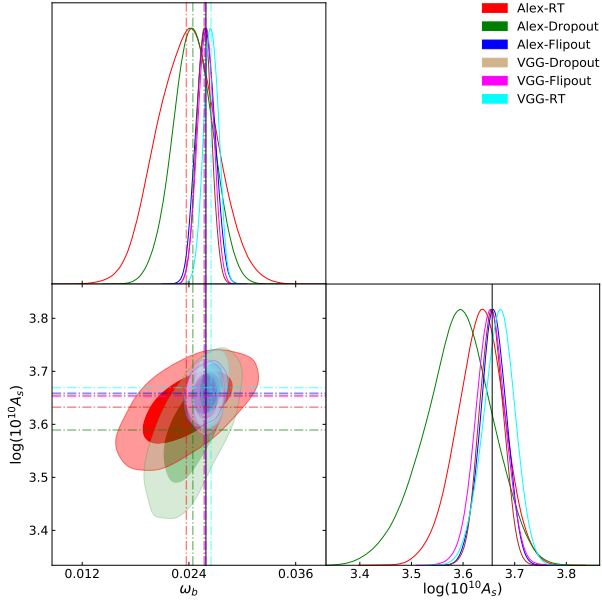


FIG. 19. Minimal base- Λ CDM 68% and 95% parameter constraint contours from our synthetic CMB dataset using Flipout with Alexnet (blue), VGG (magenta); Dropout with Alexnet (green), VGG (orange); and RT with Alexnet (red), VGG (cyan) architectures. The diagonal plots are the marginalized parameter constraints, the dashed lines stand for the predicted values and the black solid line corresponds to the true values $\omega_b = 0.02590$, $\log(10^{10} A_s) = 3.65653$.